High-Temperature Materials

SCIEPublish

Review

Friction and Contact Mechanics of Nuclear Graphite in High-Temperature Gas-Cooled Reactors: A Review

Tiezhong Lu, Nan Gui *, Zeliang Chen, Minghao Si and Shengyao Jiang

Institute of Nuclear and New Energy Technology, Collaborative Innovation Center of Advanced Nuclear Energy Technology, Key Laboratory of Advanced Reactor Engineering and Safety, Ministry of Education, Tsinghua University, Beijing 100084, China; tiezhonglu@163.com (T.L.); chen-zl20@mails.tsinghua.edu.cn (Z.C.); mhs@163.com (M.S.); jiangshy@tsinghua.edu.cn (S.J.)

* Corresponding author. E-mail: guinan@mail.tsinghua.edu.cn (N.G.)

Received: 3 June 2026; Revised: 13 July 2026; Accepted: 17 August 2026; Available online: 4 September 2026

ABSTRACT: The high-temperature gas-cooled reactor (HTGR), as a preferred reactor type for Generation IV nuclear energy systems, widely employs nuclear-grade graphite in its core as the moderator, structural material, and matrix of fuel elements. The friction coefficient between graphite components and the contact stiffness of spherical fuel elements directly affect the structural integrity of the core, the flow characteristics of the pebble bed, and the design of the fuel handling system, serving as critical mechanical parameters for ensuring reactor safety and economic operation. This paper systematically reviews the preparation processes and multi-scale microstructural features of nuclear graphite for HTGRs and summarizes the current research status in two directions: the friction coefficient and the contact stiffness of nuclear graphite. In the field of tribology, the influencing mechanisms of intrinsic factors such as grain size and porosity, as well as extrinsic factors such as ambient atmosphere, temperature, load, and sliding velocity, on the friction behavior of graphite are analyzed with emphasis. The controversies and applicable conditions of the surface energy mechanism and the dangling bond mechanism are discussed. In terms of contact mechanics, the development of asperity models from the Hertz contact and Abbott-Firestone (AF) model to the Kogut-Etsion finite-element based fitting is summarized, along with the evolution from the Greenwood-Williamson (GW) statistical model to the Majumdar-Bhushan (MB) fractal contact model. Experimental methods for measuring stiffness coefficients—namely, the interface displacement method, the impact method, and the acoustic method—are reviewed. On this basis, the severe scarcity of nuclear graphite mechanical data under in-core conditions, such as high temperatures and inert atmospheres, is highlighted. Two systematic experimental works dedicated to graphite materials for HTGRs are integrated: the first measurements of the static and dynamic friction coefficients of isostatically pressed nuclear graphite BG80 in a high-purity helium environment from 25 to 1300 °C, revealing a four-stage variation of the friction coefficient with temperature; and the first acquisition of the temperature dependence and irreversible evolution characteristics of the stiffness coefficient of spherical fuel elements in high temperature helium. These works fill the gaps in fundamental data and can provide quantitative parameter inputs and theoretical support for HTGR core design, pebble-bed flow simulations, and safety analyses.

Keywords: High temperature gas cooled reactor; Nuclear graphite; Friction coefficient; Contact stiffness; Fuel element; Fractal contact model

© 2026 The authors. This is an open access article under the Creative Commons Attribution 4.0 International License (https://creativecommons.org/licenses/by/4.0/).

1. Introduction

Driven by the goals of "carbon peaking and carbon neutrality", nuclear energy, with its high energy density and near-zero carbon emissions during operation, has become an essential base-load power source in the future energy mix [1]. From experimental prototypes in the 1950s to Generation III advanced light water reactors, nuclear reactor technology has evolved to Generation IV, which is characterized by inherent safety, economic competitiveness, and proliferation resistance (Table 1). The Generation IV International Forum (GIF), established in 2001, selected six candidate reactor types, among which the Very High Temperature Reactor (VHTR) and its transitional type, the High Temperature Gas Cooled Reactor (HTGR), are considered among the most promising because they use helium cooling, TRISO (tristructural isotropic) coated particle fuel, and a graphite core, endowing them with the inherent safety feature of no core meltdown even under loss of all coolant and unattended conditions [2].

Table 1. Six Gen IV Nuclear Reactor Types.

Reactor Type	Coolant	Characteristics	Temperature Range	Main Applications	Fuel Cycle Mode
Gas Cooled Fast Reactor (GFR)	Helium/CO_2	High pressure	850 °C	Electricity generation, Hydrogen production	Closed cycle
Lead Cooled Fast Reactor (LFR)	Lead/Lead bismuth	Atmospheric pressure	480–570 °C	Electricity generation, Hydrogen production, Nuclear waste treatment	Closed cycle
Molten Salt Reactor (MSR)	Molten salt	Atmospheric pressure	700–1000 °C	Electricity generation, Hydrogen production, Nuclear waste treatment	Closed cycle
Supercritical Water Cooled Reactor (SCWR)	Water	High pressure	510–625 °C	Electricity generation	Open cycle
Sodium Cooled Fast Reactor (SFR)	Sodium	Atmospheric pressure	500–550 °C	Electricity generation, Nuclear waste treatment	Closed cycle
Very High Temperature Reactor (V/HTR)	Helium	High pressure	900–1000 °C	Electricity generation, Hydrogen production	Open cycle

China holds a leading international position in HTGR technology. The 10 MW High Temperature Gas Cooled Test Reactor (HTR-10) (Figure 1, [3]), independently designed by the Institute of Nuclear and New Energy Technology of Tsinghua University, reached criticality in 2000 and full power operation in 2003, and successfully conducted three experiments demonstrating inherent safety, including station blackout and main helium blower shutdown. Taking HTR-10 as a prototype, the world's first modular HTGR commercial demonstration plant, HTR-PM, began construction in Rongcheng, Shandong Province, in 2012, was connected to the grid in December 2021, and formally entered commercial operation after completing a 168-h continuous operation assessment in December 2023, signifying that China has fully mastered the complete technology of modular HTGRs [1].

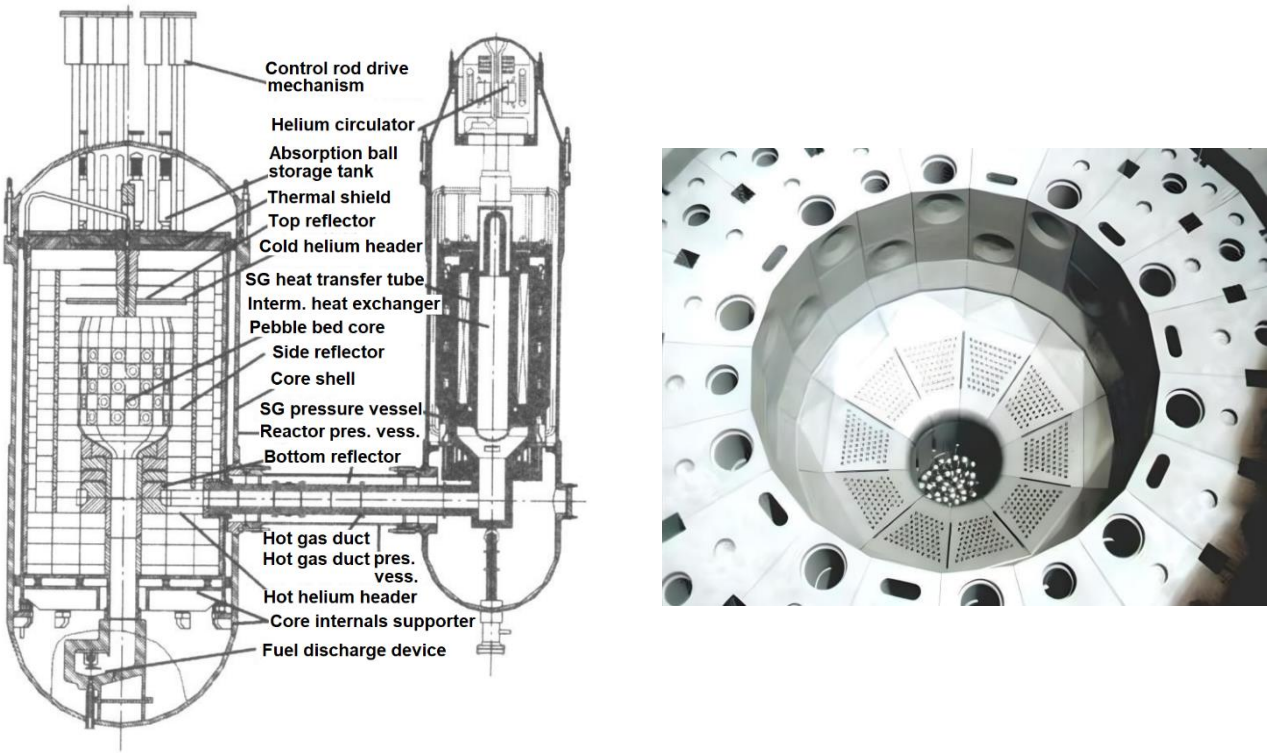

Figure 1. HTR-10 Reactor Structure.

Graphite plays an irreplaceable role in HTGRs because of its excellent neutron moderating power (moderating ratio ~200), high temperature mechanical strength (strength increases with temperature up to 2500 °C), high thermal conductivity (~125 W/(m·K)), very low thermal expansion coefficient (<4.5 × 10^{-6} /K), and good dimensional stability under irradiation [4]. In HTR-PM (Figure 2), approximately 1200 tons of structural graphite and about 80 tons of matrix graphite for fuel elements are used, constituting virtually all components inside the core except the fuel particles and control materials. The contact interface mechanical behavior of these graphite components—including the friction coefficient between graphite surfaces and the contact stiffness of spherical fuel elements—directly determines the packing structure of the pebble bed, its flow characteristics, the coolant flow field distribution, and the design parameters of the fuel handling system, which are crucial to reactor safety and performance [5].

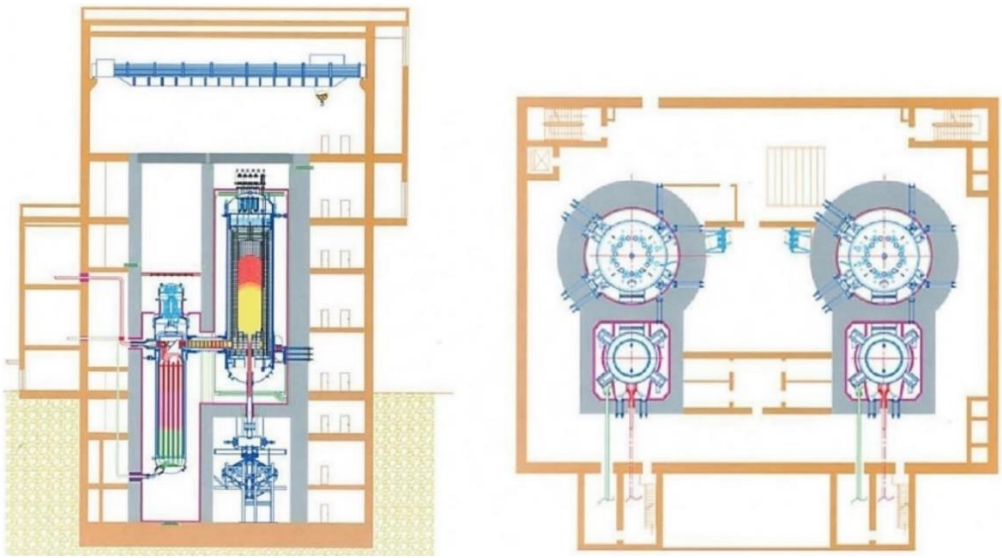

Figure 2. HTR-PM demonstration NPP design philosophy.

However, owing to the experimental challenges posed by the harsh conditions of high temperature, high purity helium environment, and irradiation, research on the friction coefficient and contact stiffness of nuclear graphite specifically for HTGRs has long been extremely scarce. Most of the available data were obtained from ordinary industrial graphite under room temperature air conditions and cannot directly support the precise design requirements of the core. This paper, by integrating two recent systematic experimental studies targeting this field, starts from the material characteristics of nuclear graphite, comprehensively reviews the current state of research on graphite tribology and contact mechanics, and systematically presents the latest experimental findings and mechanistic analyses of the friction coefficient of nuclear graphite and the stiffness coefficient of fuel spheres in a high temperature helium environment.

2. Nuclear Graphite Materials in HTGRs

2.1. HTGR Development and the Application of Graphite

Brief History of HTGRs

The technological origin of HTGRs can be traced back to the 1950s' Magnox gas cooled reactors, which used natural uranium as fuel and carbon dioxide as coolant, and subsequently evolved through Advanced Gas cooled Reactors (AGR) to advanced reactors cooled by helium and moderated by graphite. Internationally, experimental and prototype reactors such as the Dragon reactor in the UK, the AVR and THTR-300 in Germany, the HTTR in Japan, and the GT-MHR cooperatively developed by the USA and Russia have validated the feasibility of HTGRs from an engineering perspective [6]. HTR-PM adopts two pebble bed modular reactors coupled to a single steam turbine generator set, with the core loaded with approximately 420,000 spherical fuel elements of 60 mm diameter. The designed core outlet temperature is 750 °C, and the thermal power is 250 MWth [7].

Graphite performs three main functions in HTGRs [8,9]:

(1) Forming the macroscopic structure of the core, including the reflector, thermal insulation layers, neutron shielding, and guide channels for control rods and absorber ball shutdown systems;
(2) Constructing the pebble bed core and the circulation channels for spherical fuel elements, constraining the orderly flow of fuel spheres, and ensuring a uniform helium coolant flow field distribution;
(3) Serving as a heat sink under accident conditions, where graphite components and carbon bricks can absorb substantial decay heat and play a key role in the residual heat removal path.

The friction behavior at graphite interfaces directly affects the above functions: friction between fuel spheres and structural graphite can generate graphite dust, which, once accumulated to a certain extent, may impact normal reactor operation [10]; the friction force between fuel spheres in the pebble bed is a critical parameter for calculating the packing structure and flow characteristics, directly determining the boundary conditions for neutronics and thermal hydraulic calculations [11]; simultaneously, the friction coefficient is a core input for optimizing the design of the fuel handling system [12].

2.2. Preparation and Microstructure of Nuclear Graphite

Nuclear graphite is a type of artificial graphite produced through specific raw material selection and optimized preparation processes, with performance requirements far exceeding those of ordinary industrial graphite: besides meeting nuclear purity (extremely low content of neutron poisons such as boron and cadmium), it must possess high density (>1.7 g/cm^3), good isotropy, and excellent irradiation resistance [13].

The preparation process includes raw material selection, mixing and kneading, forming, carbonization, graphitization, and purification (Figure 3). The filler usually employs graphitizable carbonaceous precursors such as petroleum coke, pitch coke, or Gilsonite coke; coal tar pitch is mostly used as the binder, which is converted into solid carbon bridges connecting the filler particles at high temperatures.

Impregnation–carbonization cycles are utilized to increase the density of the green body. The forming process has a decisive influence on anisotropy: extrusion tends to align the long axes of grains along a plane perpendicular to the extrusion axis, producing one with grain (WG) direction and two against grain (AG) directions; molding produces two WG and one AG directions; whereas isostatic pressing applies pressure uniformly in all directions, yielding products with extremely low anisotropy and is therefore widely adopted for modern nuclear graphite. Graphitization treatment is performed at 2500–3000 °C, transforming carbon atoms from a short range ordered amorphous state to a long range ordered hexagonal layered crystalline state, eliminating defects and improving thermal conductivity. Purification usually employs high temperature halogen gases to remove impurities such as boron [14].

The microstructure of nuclear graphite exhibits typical multiscale characteristics [15]. At the macroscopic level, it consists of millimeter-sized filler particles, a binder phase, and pores (total porosity ~20%) (Figure 4, [16]); the type and particle size distribution of the filler determine the texture of the graphite. At the mesoscopic level, polarized light microscopy can reveal isochromatic domains—regions where crystallite orientations are roughly aligned—ranging in size from micrometers to tens of micrometers; meanwhile, calcination cracks and Mrozowski cracks are visible (Figure 5, [16]). These microcracks are generated by the anisotropic shrinkage of microcrystallites during cooling and play an important regulatory role in the mechanical and thermal behavior of graphite [17]. At the atomic scale, carbon atoms form hexagonal network planes through sp^2 hybridization. Within the plane, strong covalent bonds (bond length 0.2461 nm) prevail, while the interlayer spacing is 0.3354 nm, with the layers held together by weak van der Waals forces. This strong-in-plane/weak-out-of-plane bonding gives graphite crystals significant anisotropy, with strength and elastic modulus parallel to the basal plane being much higher than those perpendicular to it [18]. Furthermore, high resolution transmission electron microscopy has revealed finer features such as turbostratic structures, quinoline insolubles, and wrinkled structures. These microstructures can evolve under irradiation and affect the macroscopic properties of graphite [19,20].

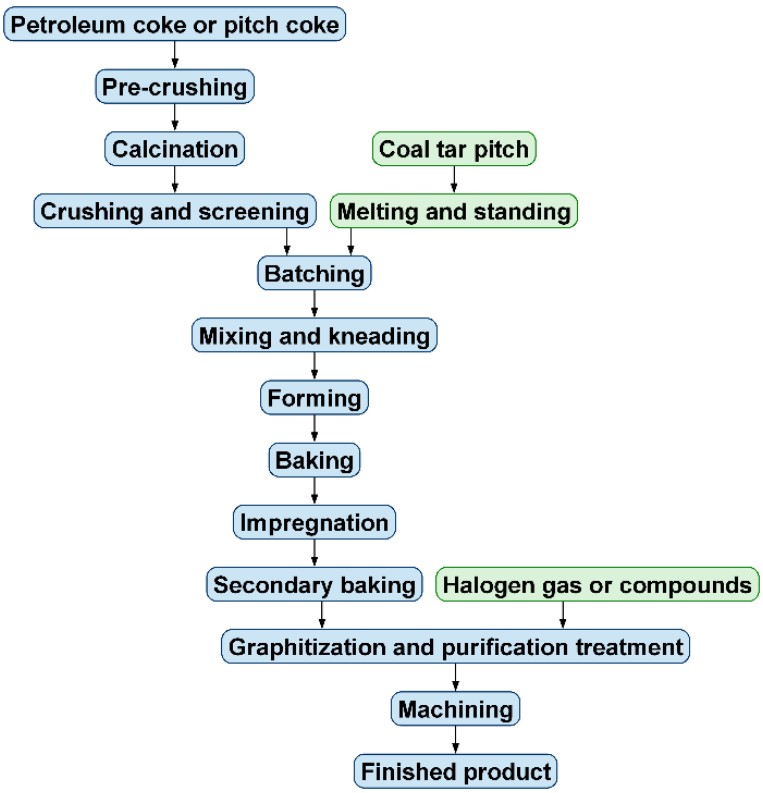

Figure 3. Nuclear Graphite Manufacturing Process Flowchart.

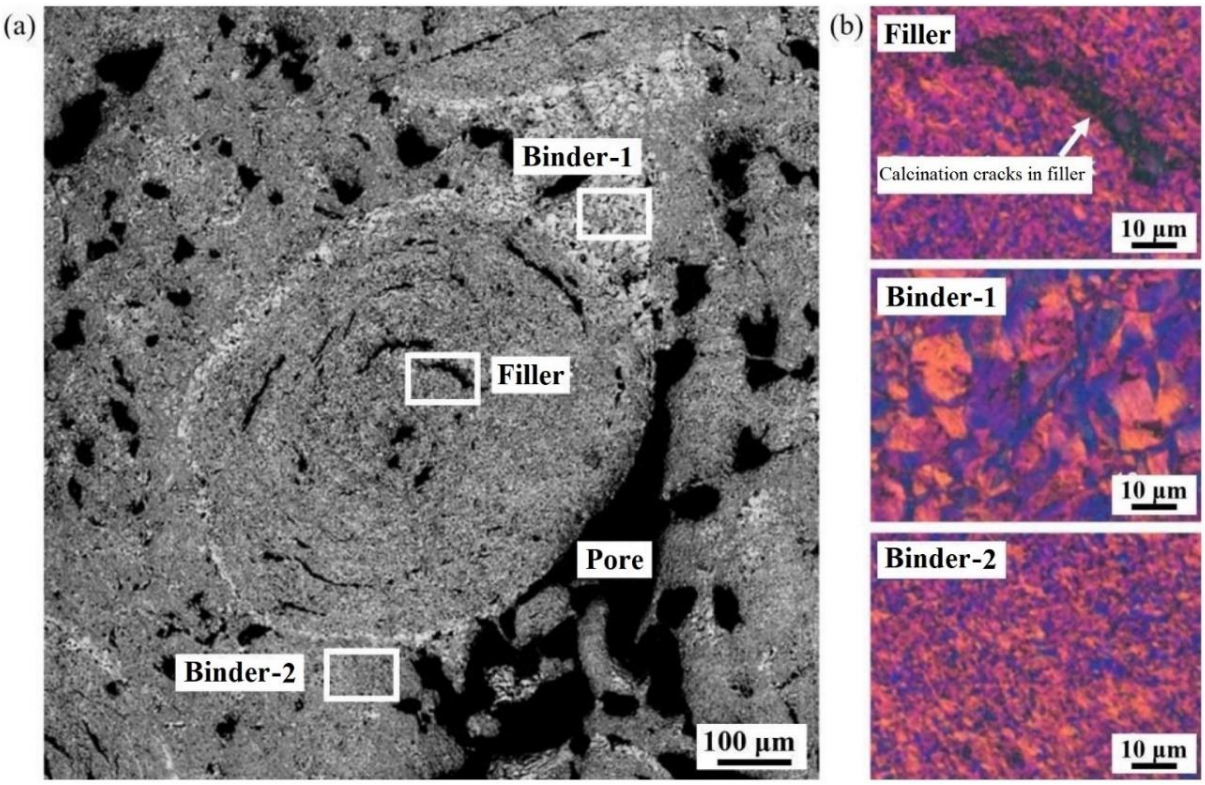

Figure 4. Optical microscopy images of Gilscocarbon [16]. (**a**) Microstructure at 100 µm scale revealing the filler, binder phases, and pores. (**b**) Magnified views (10 µm scale) of selected areas, highlighting calcination cracks within the filler and the characteristic textures of Binder-1 and Binder-2.

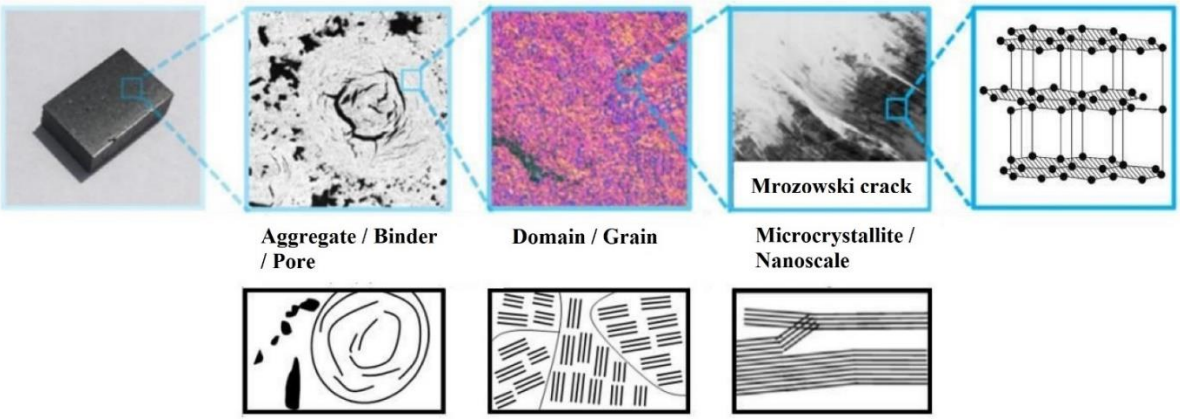

Figure 5. Schematic diagram of the multiscale structure of graphite.

2.3. Spherical Fuel Elements and Their Mechanical Requirements

Both HTR-10 and HTR-PM adopt molded spherical fuel elements, which are fabricated by a quasi isostatic pressing method in silicone rubber molds [21]. The element consists of an inner fuel zone of 50 mm diameter and an outer fuel free shell approximately 5 mm thick, with the matrix material the same in both zones and with no physical interface. The matrix is typically composed of 64% natural graphite powder, 16% artificial graphite powder, and 20% phenolic resin [22]. TRISO coated fuel particles (Figure 6) are homogeneously dispersed in the fuel zone at a volume fraction of only 5–10%; therefore, the overall mechanical behavior of the fuel sphere can be approximately treated as that of a homogeneous solid graphite sphere [5].

In the core, spherical fuel elements bear their own weight and the mechanical loads transmitted by the overlying pebble bed. Nuclear graphite is a typical quasi brittle material with no obvious linear segment on the stress–strain curve and residual stress upon unloading; however, during subsequent loading cycles after experiencing a certain maximum load, the material exhibits stable elastic hysteretic behavior, and the gradient of the reloading curve can be used to define the stiffness coefficient under those conditions [23]. This stiffness coefficient is a key parameter for quantitatively evaluating the deformation of fuel spheres, calculating the contact force chain distribution in the pebble bed, and performing whole core structural integrity simulations. Nevertheless, to date, experimental measurements of the contact stiffness of fuel spheres under actual high temperature helium environments have been lacking, creating an urgent need to establish reliable measurement and analysis methods.

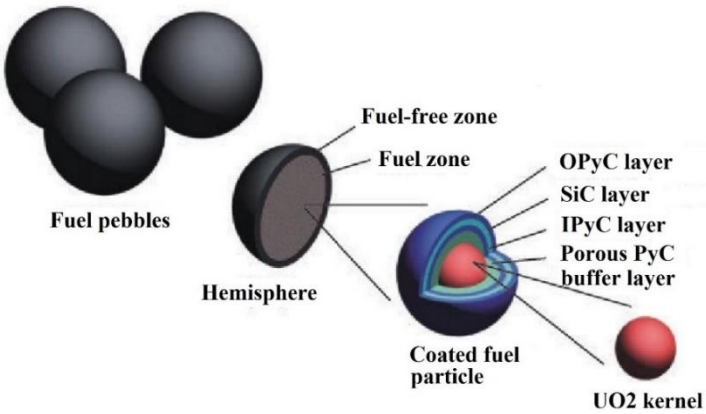

Figure 6. Schematic of an HTGR spherical fuel element with embedded TRISO particles.

3. State of the Art in Graphite Friction Coefficient Research

Factors affecting the friction coefficient of graphite can be divided into two categories: intrinsic and extrinsic. Intrinsic factors, determined by the type of raw materials and the preparation process, are fixed before the graphite components are put into service; extrinsic factors are the dominant variables that govern the dynamic changes in friction behavior during reactor operation.

3.1. Influence of Intrinsic Factors

Intrinsic properties of graphite, such as grain size, porosity, and degree of graphitization, significantly affect its friction performance. Zhou Qiang et al. pointed out that graphite micropowder with an average particle size of 4–5 μm exhibits the best lubricating effect; larger grains induce an abrasive effect that increases the friction coefficient, whereas very fine particles tend to form an adsorbed film on the friction surface, also leading to an increase in the friction coefficient [24]. Luo et al. used a standard friction tester to compare the friction behavior of graphites with different grain sizes in air and helium, and found that in room temperature air, the friction coefficient of fine grained graphite decreased with increasing load, while coarse grained graphite showed the opposite trend. In a helium environment, the friction coefficient of fine grained graphite increased compared with that in air, whereas that of coarse grained graphite was close to the value in air, indicating a coupling effect between atmosphere and grain size [25]. Further mechanistic analysis indicated that the adsorbed film on the graphite surface plays a dominant lubricating role in air, whereas in helium, friction relies on microdisplacement lubrication of graphite crystals on the friction surface [26]. Zhu et al. found that carbon materials with a higher degree of graphitization are more likely to form a transfer lubricating film on the friction surface, thereby reducing the friction coefficient [27]. Xu prepared graphite using pitch coke as the filler and confirmed that the friction coefficient gradually

increases as the filler grain size decreases, whereas the introduction of natural graphite can further reduce the friction coefficient [28]. Skinner et al. used a scanning electron microscope to observe the sliding of a tungsten needle on the basal and prismatic faces of graphite single crystals and found that the friction coefficient on the prismatic face could be 5 to 20 times higher than that on the basal face, visually demonstrating the tremendous influence of graphite crystal orientation on friction [29].

Moreover, the pore structure also has an important impact on friction behavior. Liu et al. prepared high density graphites with different pore structures using isostatic pressing, compression molding, and thermoforming methods, and found that as the fractal dimension increases, both the friction coefficient and wear amount of graphite increase; thermoformed graphite, with the highest degree of graphitization (75.4%) and the lowest total porosity (15.08%), exhibited the best overall tribological performance [30]. For isotropic nuclear graphite used in HTGRs, the above intrinsic factors are already determined during preparation, and the key variables affecting the friction coefficient during core operation are the extrinsic environmental conditions.

3.2. Influence of Ambient Atmosphere and Lubrication Mechanisms

The ambient atmosphere is the most significant extrinsic factor affecting the friction coefficient of graphite, and two theoretical hypotheses—the surface energy mechanism and the dangling bond mechanism—are mainly used to explain its action [31].

The surface energy mechanism explains friction behavior based on the differences in surface energy of different crystal faces of graphite. In a vacuum, the surface energy of the prismatic face of graphite is as high as 5 J/m^2, whereas that of the basal face is only 0.1–0.2 J/m^2, meaning the prismatic face has higher adsorption activity [32]. When graphite slides against graphite, the high surface energy in a vacuum results in strong physical adsorption between the two friction surfaces, leading to a very high friction coefficient. In active gases (oxygen, water vapor, organic vapors), gas molecules form a physically or chemically adsorbed passivation film on the graphite surface, reducing the surface energy and weakening the adsorption interaction between the friction surfaces, thereby decreasing the friction coefficient [33]. The classic study by Savage et al. found that when the water vapor partial pressure reached approximately 3 mmHg, the friction coefficient of graphite decreased significantly and the wear rate dropped below 10^{-4} mm^3/s; oxygen required a higher partial pressure to achieve a similar effect, whereas the friction coefficient and wear rate in gases such as nitrogen and carbon monoxide were similar to those in vacuum [34]. In inert gases (helium, argon), gas atoms intercalate between the graphite layers, weakening the van der Waals forces between layers, making the graphite lamellae more easily separated and rearranged under frictional shear forces, and causing the basal planes to tend to align parallel to the sliding direction, thereby reducing the friction coefficient to an even lower level than in active gases [35]. In summary, according to the surface energy mechanism, the order of the friction coefficient of graphite from highest to lowest in different atmospheres is: vacuum > oxygen > air > water vapor > inert gas [32] (Figure 7).

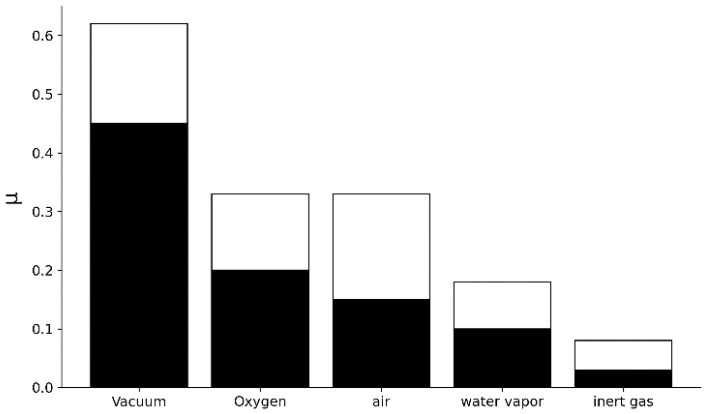

Figure 7. Friction coefficient of graphite in various atmospheres: vacuum, oxygen, air, water vapor, and inert gas. The white region represents the range of fluctuation of the friction coefficient [32].

The dangling bond mechanism explains friction from the perspective of chemical reactions between active carbon atoms generated by friction and gas molecules (Figure 8). During friction, a large number of active carbon atoms with dangling bonds are generated on the graphite surface due to lattice fracture. In vacuum or under inert gases, the dangling bonds on the two friction surfaces directly form "carbon–carbon" bonds, which require extremely high shear forces to break, manifesting as a very high friction coefficient. In oxygen, the dangling bonds react with oxygen to form "carbon–oxygen–carbon" bond bridges, or form oxidized groups on the same surface, weakening the direct bonding between the surfaces and significantly reducing the friction coefficient [36]. In water vapor, carbon atoms tend to form "carbon–oxygen–hydrogen" groups on the same surface, also reducing interlayer adhesion [37]. Xiao et al. used highly oriented pyrolytic graphite (HOPG) in comparative experiments and measured an average friction coefficient of 0.25 perpendicular to the basal plane and only 0.1 parallel to the basal plane. When the atmosphere was changed from air to nitrogen containing water vapor, the friction coefficient in both directions decreased, with a larger decrease in the perpendicular direction. Through X ray photoelectron spectroscopy, they confirmed the difference in the amount of chemisorbed oxygen combined with dangling bonds on the two surfaces, providing strong support for the dangling bond mechanism [36].

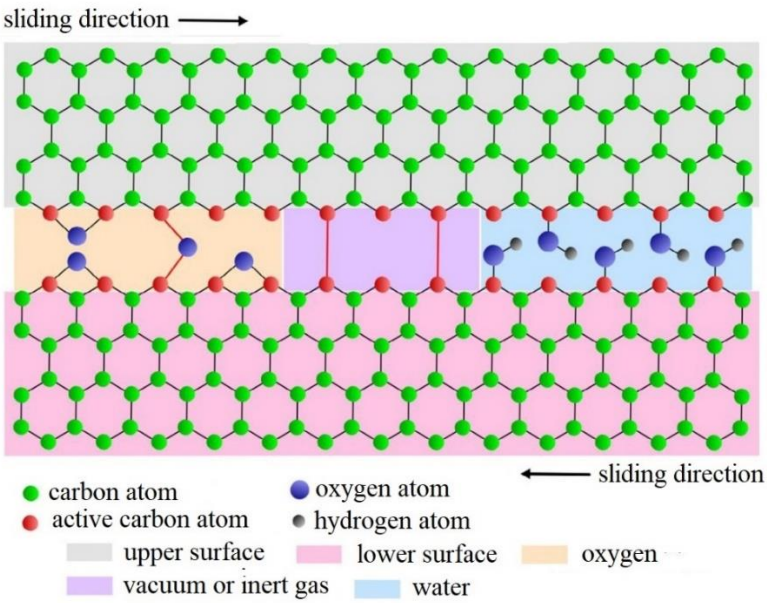

Figure 8. Schematic diagram of the dangling bond mechanism between two contacting surfaces during friction in vacuum or inert gas, oxygen, and water vapor environments.

Both mechanisms are effective in explaining the reduction of friction in active gas atmospheres; the divergence mainly appears in the case of inert gases: the surface energy mechanism predicts a friction coefficient lower than that in vacuum, whereas the dangling bond mechanism predicts a high friction close to that in vacuum. Numerous experiments have shown that the friction coefficient of graphite in inert gas atmospheres is significantly lower than in vacuum and even lower than in active gas atmospheres. Therefore, under inert gas conditions, the surface energy mechanism is more persuasive [38].

However, contrary to the conventional expectation that inert gases promote lubrication, the literature reveals a more nuanced and often contradictory frictional behavior of graphite in argon. Some studies report remarkably high friction coefficients in such environments. For instance, research on turbostratic graphite under argon has documented coefficients ranging from a surprisingly low 0.15 to an ultralow 0.002, a phenomenon attributed to the self organization and superficial mobility of crystallites at the contact interface. However, the same study found that friction was fairly high (0.32–0.42) when tests were performed under nitrogen, highlighting the gas specific nature of the effect [39].

The mechanistic origins of these varied friction coefficients are rooted in the surface chemistry of graphite. The tribological behavior of graphite in inert environments, particularly argon, is governed by a delicate balance between surface chemistry and mechanical conditions. Paulmier and Zaidi established that the high friction coefficient of graphite in vacuum or inert gases stems from the creation of active "dangling bonds" at the contact interface during sliding [33]. They demonstrated that while freshly crushed graphite exhibits a low concentration of free radicals (5%), exposure to atomic hydrogen produces two opposing effects: a low concentration increases chemical activity and friction, whereas a high, near saturation concentration passivates the surface, reducing both friction and wear. Complementing this, Wild and Mack provided practical engineering data for nuclear reactor components, reporting a notably high friction coefficient of 0.35–0.5 for CrC-coated steel sliding in argon, highlighting the challenging nature of such atmospheres for moving mechanical systems [40]. Collectively, these works underscore that friction in argon is not a fixed material property but a complex response to the interplay of surface passivation, sliding dynamics, and contact history, with the inert gas facilitating both ultra low friction under mild conditions and severe adhesion when surface activation outpaces passivation.

3.3. Influence of Temperature

The influence of temperature on the friction coefficient of graphite depends on the atmospheric environment and exhibits markedly different patterns.

In a vacuum environment (Figure 9), the friction coefficient of graphite decreases monotonically as temperature increases. The increase in temperature enlarges the interlayer spacing of graphite crystals, making it easier for graphite microcrystallites on the friction surface to undergo relative sliding and orientation rearrangement, forming a lubricating film with basal planes parallel to the sliding direction, thereby reducing the friction coefficient [41,42].

In inert gases (e.g., helium, argon), the friction coefficient of graphite likewise decreases with increasing temperature (Figure 10). Inert gas atoms do not participate in chemisorption, but as the temperature rises, the thermal motion of the atoms intensifies, and combined with the thermal expansion of the graphite interlayer spacing, gas atoms can more readily intercalate in large numbers between the graphite layers, further weakening the interlayer bonding and enhancing the lubrication effect [43]. However, a study by Driesner et al. found that above 1500 °C the friction coefficient of graphite no longer continued to decrease but rather slightly rebounded, which was attributed to the onset of obstruction of relative sliding by fine particles exfoliated from the graphite at high temperatures [44].

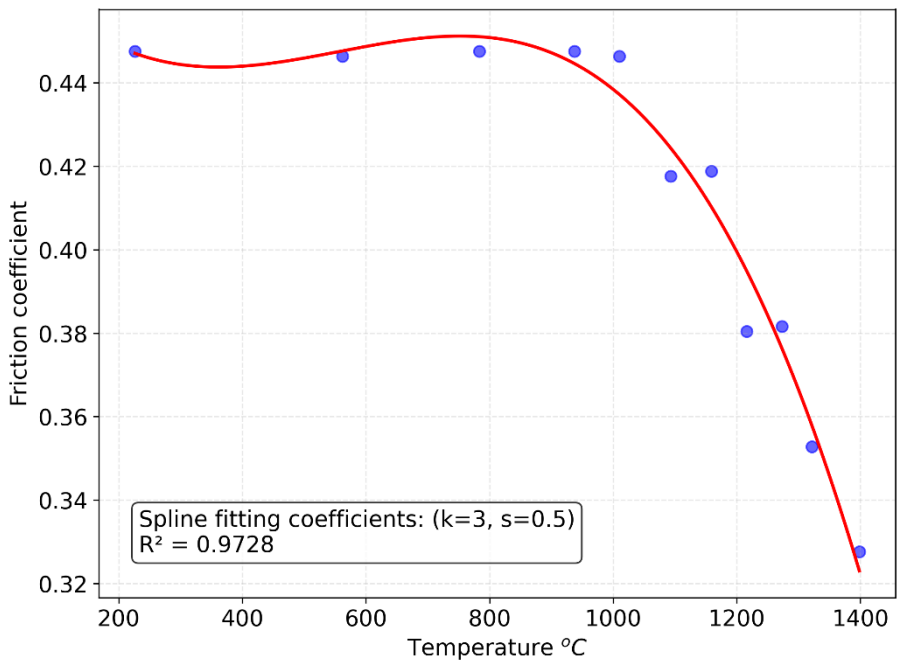

Figure 9. Figure of friction coefficient between graphite surfaces as a function of temperature in vacuum environment.

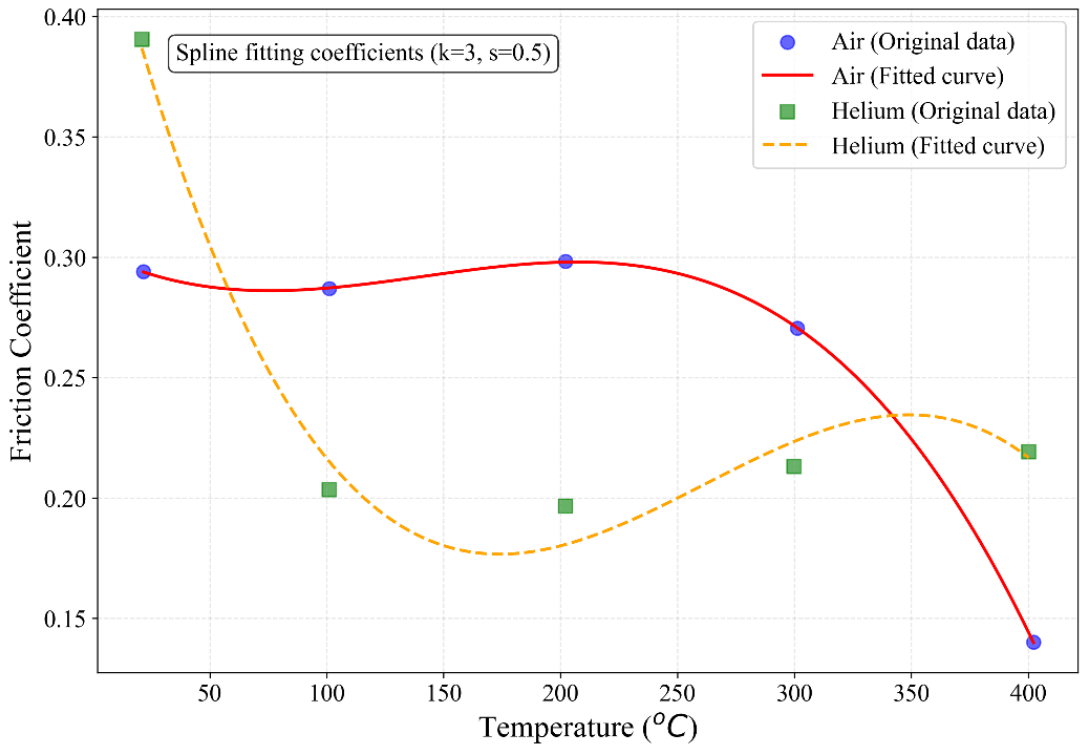

Figure 10. Figure of the friction coefficient between graphite surfaces as a function of temperature in air and helium environments.

In active gases (air, oxygen, water vapor), the effect of temperature is more complex. The friction surface of graphite relies on physically adsorbed gas molecules (mainly water and oxygen molecules) to provide lubrication. As the temperature increases, the physically adsorbed layer gradually desorbs and fails. Lancaster found that when the friction surface temperature reached 150–185 °C, the lubricating adsorbed film began to collapse and the friction coefficient increased [44]. Zaidi et al. experimentally confirmed that at 200 °C, approximately 50% of the water molecules adsorbed on the graphite surface underwent

desorption, and these water molecules are the key source of low friction of graphite in an air environment [32]. Therefore, in active gases, the friction coefficient of graphite generally increases with increasing temperature. However, around 400 °C, some experiments have observed another decrease in the friction coefficient because, at this temperature, the rate of the thermal chemical reaction between graphite and oxygen is sufficiently high, and the generated CO and CO_2 gases cover the nascent friction surface and provide temporary lubrication [45,46].

3.4. Influence of Normal Load and Sliding Speed

The influence of load on the friction coefficient of graphite exhibits a two stage characteristic. When the load is low and the graphite is within the elastic deformation range, as the load increases, the rate of increase in the real contact area of the friction surface lags behind the rate of increase in load. This means that the increase in the adhesion force component is smaller than that of the shear force component, resulting in a decrease in the friction coefficient [47]. When the load further increases to the point of causing plastic deformation or particle exfoliation on the graphite surface, plastic flow and abrasive wear lead to an increase in the friction coefficient, with furrows and severe wear characteristics forming on the friction surface [48,49].

The influence of sliding velocity is related to a "critical sliding velocity". In inert gases, the friction coefficient under low speed sliding is relatively low because the gas has sufficient time to enter between the graphite crystal layers and form a lubricating film. When the sliding velocity exceeds the critical value, the friction surface is rapidly stripped, and the lubricating film cannot form or recover in time, causing the friction coefficient to increase sharply [50]. In active gases, high speed sliding leads to a rapid temperature rise on the friction surface, resulting in the desorption and failure of the adsorbed gas film, thereby increasing the friction coefficient [51].

On the whole, most friction tests in the existing literature were conducted at room temperature. Friction data for graphite at high temperatures (>400 °C) and in inert atmospheres (especially helium) are extremely limited and show a large scatter. As shown in Table 2, the experimental results for the friction coefficient of graphite in helium range from roughly 0.02 to 0.40, with almost no data in the high temperature range. This represents a significant gap relative to the actual operating conditions of HTGRs and is precisely the starting point for the latest systematic experimental research reviewed in this paper.

Table 2. Overview of International High Temperature Gas Cooled Reactor Development.

Year of Operation	Country	Reactor Model	Power	Fuel Element
1964	United Kingdom	Dragon	20 MWth	Graphite coated ceramic particles
1967	United States	Peach Bottom	40 MWe	Prismatic fuel element
1967	Germany	Pebble Bed HTGR AVR	15 MWth	Spherical fuel element
1976	United States	Fort St. Vrain	330 MWe	Prismatic fuel element
1985	Germany	Thorium High Temperature Pebble Bed Reactor THTR-300	300 MWe	Spherical fuel element
1998	Japan	High Temperature Engineering Test Reactor HTTR	30 MWth	Prismatic fuel element
—	Germany	Modular High Temperature Gas Cooled Reactor HTR-Module	200 MWth	Spherical fuel element
—	United States	Modular High Temperature Gas Cooled Reactor MHTGR	250 MWth	Prismatic fuel element
—	United States/Russia	Gas Turbine Modular Helium Reactor GT-MHR	285 MWe	Prismatic fuel element

—	Japan	Gas Turbine High Temperature Reactor GTHTR	600 MWth	Prismatic fuel element
—	South Africa	Pebble Bed Modular Reactor PBMR	100 MWe	Spherical fuel element
2000	China	10 MW High Temperature Gas cooled Test Reactor (HTR-10)	10 MWt	Spherical fuel element
2021	China	High Temperature Gas cooled Reactor—Pebble bed Module (HTR-PM)	200 MWe	Spherical fuel element

4. State of the Art in Graphite Contact Stiffness and Interface Mechanics Modeling

The contact stiffness of spherical fuel elements is essentially a macroscopic characterization of the contact deformation of two rough solid surfaces under a certain normal load. Its theoretical modeling involves a cross scale mechanical analysis from a single asperity to the entire rough interface.

4.1. Asperity Contact Models

The contact mechanics of asperities originates from the elastic contact theory proposed by Hertz in 1881, which assumes the asperity to be a homogeneous, isotropic elastic sphere and provides an analytical relationship between normal load and deformation, still serving as the foundation of contact mechanics today [21] (Figure 11). When the load increases to the point where the maximum stress in the contact area reaches a threshold of the material hardness, the asperity yields. The AF model describes the behavior of an asperity in a fully plastic state, assuming that the contact load equals the product of the material hardness and the contact area [52].

Real asperities undergo an elastoplastic transition stage between elasticity and full plasticity. Chang et al. attempted to directly splice the Hertz model with the AF model, but the contact pressure was discontinuous at the critical deformation, exposing the deficiency of a simple two segment division [53]. Zhao et al. used an exponential function to smoothly connect the elastic and plastic segments, ensuring continuity of contact load and area at the critical point, but the contact stiffness remained discontinuous [54]. Xiao et al. used a low order elliptic curve to achieve three continuity boundary conditions for contact load, area, and stiffness, with high accuracy, but the mathematical form was complex and inconvenient for further coupling with the overall interface model [55].

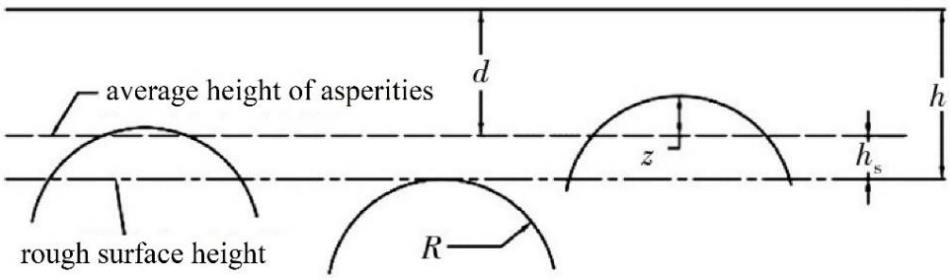

Figure 11. Asperity model of rough surface.

The development of finite element technology has provided a new approach for modeling elastoplastic contact of asperities. Based on numerous finite element simulations, Kogut and Etsion [56] subdivided the elastoplastic deformation stage into the first and second substages and fitted exponential relationships between contact load and contact area and deformation in each stage. This model, which combines high accuracy with a concise functional form, has been widely used in macroscopic contact modeling of interfaces. Jackson and Green, based on more extensive finite element calculation results, modified the expression for the critical elastoplastic deformation, offering better applicability in the large deformation stage

[57]. In addition, regarding the tangential behavior of asperities, Mindlin derived the exact solution for the tangential force and tangential deformation of an asperity under partial slip conditions based on the local Coulomb friction law, which remains the core theory for tangential contact analysis of rough surfaces [58].

4.2. Rough Surface Contact Models and Fractal Theory

Contact between actual engineering surfaces involves the collective behavior of many asperities, requiring the combination of a single asperity model with a statistical or fractal description of the surface topography.

The GW model proposed by Greenwood and Williamson is the most classic statistical contact model. It assumes that the heights of surface asperities follow a Gaussian distribution, the deformation of each asperity is independent of the others, and the contributions of all asperities are integrated to obtain the macroscopic contact load and contact stiffness [59]. The GW model is simple and practical, but its key parameters (such as asperity density, radius of curvature, *etc.*) depend on the resolution and sampling length of the measuring instrument, suffering from a "measuring instrument dependence" problem and lacking universality across different machined surfaces.

Fractal contact models exploit the self-affine fractal characteristics of rough surfaces, using a scale-invariant Weierstrass–Mandelbrot (W–M) function (Figure 12) to describe the surface topography, fundamentally overcoming the scale dependence problem of statistical models. Majumdar and Bhushan combined the W–M function with asperity contact mechanics and proposed the classic MB model, establishing fractal scaling relationships among interface contact load, contact area, and contact stiffness [60,61]. Wang and Komvopoulos further corrected the distribution function of the truncated contact area of asperities in the MB model by introducing a domain extension coefficient, improving calculation accuracy [62]. Yan and Komvopoulos extended the MB model to three dimensional isotropic rough surfaces, providing a more precise description of normal deformation [63]. Subsequently, Zhang, Tian, and others conducted a series of studies on the normal and tangential contact stiffness of mechanical joints based on the MB model and elastoplastic asperity models, and proposed the virtual material method for contact interfaces—introducing a virtual material layer at the interface and setting its elastic parameters to equivalently represent the contact stiffness of the interface, which facilitates implementation in finite element analysis [64]. However, none of these models have specifically considered the unique microstructural features of nuclear graphite (such as Mrozowski cracks and pores) and the influence of high temperature environments on contact behavior. Furthermore, modeling under non-uniform interface stress distribution conditions still relies on complex pre-analysis and lacks generality.

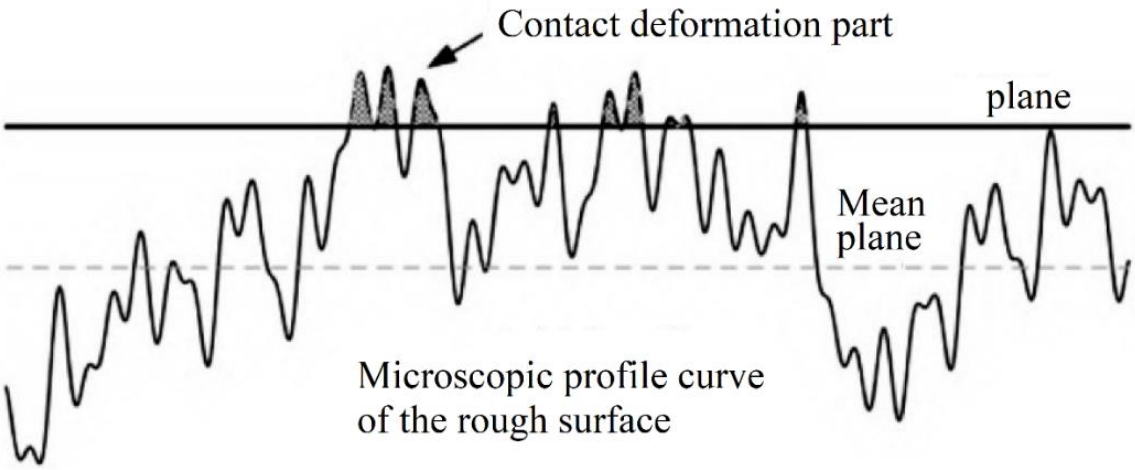

Figure 12. Rough surface characterized by the Weierstrass Mandelbrot function.

4.3. Experimental Methods for Stiffness Coefficient Measurement

There are three main types of experimental methods for measuring interface stiffness [65]:

The interface displacement method directly relies on the definition of stiffness. By measuring the relative normal displacement of the interface under different normal loads, the contact stiffness is obtained by calculating the slope of the load–displacement curve (Figure 13). The principle of this method is simple, but it imposes extremely high requirements on the proximity of the displacement measurement points to the contact interface. Displacements measured far from the interface will include deformations of the testing system and supporting structure, which require careful correction. Yuan et al. proposed an improved method to eliminate systematic errors arising when measurement points are not located directly on the interface [66].

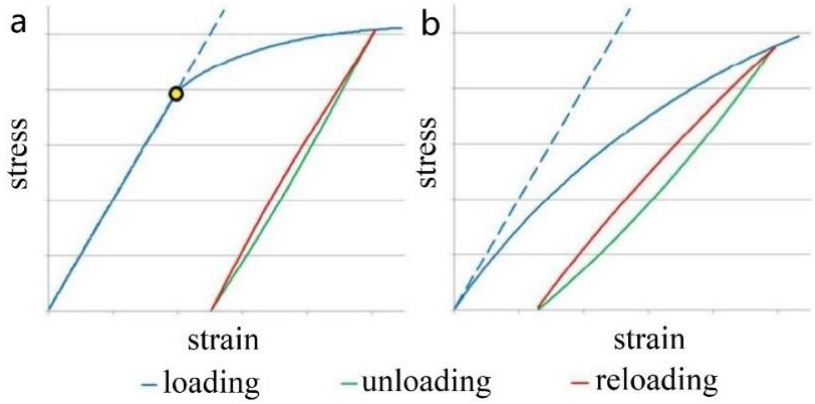

Figure 13. Schematic diagram of the stress-strain curve of the plastic material (**a**) and nuclear graphite (**b**) (The yellow circle is the yield point, and the deshed line is the elastic modulus line).

The impact test method correlates stiffness with the natural frequency and frequency response function of the structure, and the stiffness is inversely derived through experimental modal analysis. The limitation of this method lies in the need for an accurate analytical model of the vibration response, which is very difficult to obtain for complex boundary conditions [67].

The acoustic method utilizes the reflection, transmission, and nonlinear effects of elastic waves at the contact interface to characterize the interfacial contact state. Krolikowski proposed evaluating the contact stiffness by measuring the longitudinal wave transmission coefficient [68]; Dwyer-Joyce et al. measured the contact stiffness of rough surfaces through the longitudinal wave reflection coefficient and found significant plastic flow during the first loading, which tended to elastic stability after multiple loading cycles [69]. The acoustic method has advantages in nondestructive testing and online monitoring, but its application in high temperature, high pressure, and complex geometric structures still faces technical challenges such as sensor installation and signal decoupling.

4.4. Effect of Damage on the Contact Mechanical Behavior

The structural integrity of nuclear graphite in high temperature reactors is critically influenced by damage accumulation and complex stress states, as explored through complementary experimental, analytical, and numerical approaches. Jia et al. systematically investigated the failure mechanism of line contact structures (e.g., graphite brick-tenon joints) in IG11 graphite, identifying a three stage progressive failure process: initial damage accumulation leading to characteristic yielding without visible cracks, followed by crack initiation and lateral propagation when stresses satisfy the Mohr failure criterion, and finally, the formation of a secondary Y-shaped crack that precipitates complete structural failure. This staged mechanism underscores the critical role of contact geometry-induced stress concentration in

triggering damage evolution [70]. To model such damage driven failure, Zou et al. developed a unified continuum damage mechanics (CDM) model that integrates both stress-based and fracture-mechanics-based criteria. Their model successfully predicts failure under both regular and singular stress concentrations, as validated against experiments on L-shape and channel section specimens with varying corner radii, demonstrating its suitability for capturing the transition from diffuse damage to discrete crack formation [71]. Complementing these studies, Yang et al. addressed an operational challenge—molten salt infiltration in TMSR—by analyzing its influence on stress distribution in graphite components under irradiation. Their simulations revealed that dose gradients, permeation zone shapes, and areas significantly alter the principal stress fields, with peak stresses often localized at geometric centers and symmetry modifications induced by non-uniform infiltration patterns [72].

To conclude, these studies highlight that the mechanical behavior of nuclear graphite in contact is governed by a complex interplay among initial damage, stress concentrators, and environmental factors (e.g., irradiation and coolant infiltration), necessitating integrated damage models and geometry-aware stress analyses for reliable reactor core design and safety assessment.

5. Existing Problems in Research

For convenience, the following table (Table 3) summarizes the friction coefficient study.

Table 3. Summary of Graphite Friction Coefficient Studies.

Author(s)	Object of Study	Method	Atmosphere	Temperature	Load	Friction Coefficient
Fu et al. [48]	Matrix graphite of fuel element	Wear tester	Air	Room temperature	0–50 N	0.05–0.16
Li et al. [59]	Matrix graphite of fuel element	Friction and wear tester	Nitrogen	Room temperature–900 °C	5 N	0.07–0.55
Luo et al. [25]	Domestic nuclear grade graphite	SRV tester	Air	Room temperature	40 N	0.2–0.4
Luo et al. [26]	Domestic nuclear grade graphite	SRV tester	Air	Room temperature	30 N	0.26–0.43
Luo et al. [38]	Domestic nuclear grade graphite	SRV tester	Air	Room temperature	20 N	0.1–0.4
Luo et al. [45]	Domestic nuclear grade graphite	SRV tester	Air	Room temperature–400 °C	30 N	0.14–0.30
Song et al. [73]	Impregnated graphite	Ball/pin-on-disk tribometer	Air	Room temperature	10 N	0.10–0.30
Xu [28]	Zinc phosphate-impregnated carbon-graphite material	High temperature friction and wear tester	Air	Room temperature–450 °C	5 N	—
Xu et al. [74]	Graphite	High temperature friction and wear tester	Air	300–450 °C	300–400 g	—
Zhu et al. [27]	Carbon-graphite material	Vertical universal friction and wear tester	Air	Room temperature	8 MPa	0.165–0.30
Aranganathan et al. [75]	Natural graphite	Inertia dynamometer	Air	325 °C	—	0.20–0.48
Bowden et al. [76]	Graphite	Custom-built apparatus	Vacuum/Air	0–100 °C/700–1200 °C	13.5 g/17 g	0.19–0.62
Csapo et al. [50]	Graphite	Tribometer	Argon	Room temperature	5 N	0.06–0.7
Driesner et al. [43]	Graphite	Custom-built apparatus	Argon	25 °C	250 lb/in^2	0.16–0.40

Jin et al. [77]	Natural graphite/ Expanded graphite	Constant-speed tribometer	Air	100–300 °C	0.98 MPa	0.3–0.5
Kumar [39]	Graphite	Tribometer	Argon	Room temperature	2 N	0.32–0.42 (Argon), 0.002 (Water vapor)
Kumar et al. [48]	Crystalline graphite	Tribometer	Air	Room temperature	10–350 mN	0.005–0.14
Lancaster et al. [78]	Graphite	Tribometer	Air	20–260 °C	20 N	0.50
Lancaster et al. [44]	Graphite	Tribometer	Air	Room temperature	5–100 N	0.15–0.7
Lancaster [51]	Graphite	Custom-built apparatus	Air	Room temperature–350 °C	12 N	0.15–0.6
Liu et al. [30]	High-density graphite	High-speed pin-on-disk tribometer	Air	Room temperature	30 N	0.144–0.246
Morstein et al. [79]	Graphite	Microtribometer	Air	Room temperature	69 mN	0.12–0.6
Paulmier et al. [33]	Polycrystalline graphite	Custom-built apparatus	Air	1400–2100 K	100 N	0.3–0.6
Robert [80]	Graphite	Custom-built apparatus	Argon	Room temperature	4 N	0.02–0.1
Rowe [41]	Graphite	Custom-built apparatus	Argon	Room temperature–2000 °C	45 kg	0.2–0.4
Savage [34]	Graphite	Custom-built apparatus	Vacuum/Air/Water vapor	400 °C	—	Water vapor: 0.18, Vacuum: 0.8
Semenov [42]	Graphite	Custom-built apparatus	Vacuum/Argon	Room temperature–1500 °C	—	0.1–0.75
Skinner et al. [29]	Single-crystal graphite	Tungsten needle friction under SEM	Vacuum	Room temperature	1–400 mg	Basal plane: 0.005–0.02, Prismatic plane: 0.3
Stansfield [81]	Graphite	Custom-built apparatus	Argon/Air	25 °C	4.2–35.0 kg/cm^2	0.23–0.44
Vergari et al. [82]	Nuclear-grade graphite	Tribometer	Argon	Room temperature/600 °C	50 N	0.55 (RT), 0.33 (600 °C)
Xiao [36]	Highly oriented pyrolytic graphite (HOPG)	Tribometer	Argon/Water vapor	Room temperature	0.5–5 N	0.1–0.25
Zaidi et al. [83,84]	Graphite	Custom-built apparatus	Argon/Air	Room temperature	10 N	0.3–0.6
Zaidi et al. [32]	Graphite	Custom-built apparatus	Vacuum/Air/Water vapor/Inert gas	Room temperature	4 N	Vacuum: 0.6, Air: 0.3, Water vapor: 0.1, Inert gas: 0.02
Zaidi et al. [85]	Polycrystalline graphite	Custom-built apparatus	Argon	Room temperature	4 N	0.03–0.38/0.03–0.40
Zaidi et al. [86]	MoS_2 coatings	Pin-on-disk tribometer	Vacuum/helium/argon/water vapor/air	Room temperature	4.6 N	vacuum: 0.01; helium: 0.03; argon: 0.04; dry air: 0.17; water vapor: 0.30
Pape [87]	Graphene platelets (2, 6–8, 11–15 nm), nano-graphite (3–4 nm), fullerene	Reciprocating sliding tribometer; pre-rolling *vs.* no pre-rolling	Air	Room temperature	1 N (660 MPa); 2 N (830 MPa)	GPLs: 0.1–0.2; nano-graphite: 0.1–0.5; fullerene: >0.5 (up to >1.0)

Summarizing the above status, the following significant deficiencies exist in the research on the friction and contact stiffness of nuclear graphite for HTGRs:

(1) Lack of generality in research objects and scarcity of nuclear grade graphite data. The vast majority of tribology studies have used ordinary industrial graphite or natural graphite, whose grain size, purity, anisotropy, and pore structure are vastly different from those of nuclear grade graphite, making it difficult to directly transfer the conclusions. Studies specifically targeting dedicated isostatic graphite for HTGRs that meet nuclear purity and isotropy requirements are exceedingly rare (Table 2).
(2) Severe deviation of test conditions from the actual in-core environment. Most existing friction tests have been completed under room temperature air, a few have reached 400 °C, and very few have touched 1000 °C. Systematic data for the normal operating temperature range of HTGRs (250–950 °C) and accident conditions (>1600 °C) are virtually absent. Regarding the atmosphere, tests in a high purity helium environment are extremely scarce, and the reported data are highly scattered (friction coefficient 0.02–0.40), unable to provide a reliable basis for engineering design Table 2. Prior to recent work, data on the contact stiffness of fuel spheres in high temperature helium were nonexistent.
(3) A complete blank in research on irradiation effects. The graphite components inside an HTGR core will inevitably undergo lattice damage, dimensional changes, and elastic modulus evolution under neutron irradiation, which will unavoidably affect friction and contact stiffness. However, all experiments to date have been conducted on unirradiated specimens, and the coupled effects of irradiation, temperature, and atmosphere remain to be explored.
(4) Theories and models have not yet been characterized for nuclear graphite. The fractal contact models have not incorporated the unique multiscale pore and microcrack characteristics of nuclear graphite. The convenience and generality of the virtual material method for interfaces still need improvement, and the two interface mechanical quantities—friction coefficient and contact stiffness—have not yet been incorporated into a unified mechanical framework for study.

6. Latest Experimental Studies on the Mechanical Behavior of Nuclear Graphite for HTGRs

To address the above mentioned gaps, two independent systematic experimental studies have recently completed measurements of the friction coefficient of nuclear graphite and the stiffness coefficient of spherical fuel elements for HTGRs, providing for the first time continuous experimental data from room temperature up to 1300 °C in a high purity helium environment.

6.1. Friction Coefficient of Nuclear Graphite in High Temperature Helium

6.1.1. Experimental Measurements

The first study used isostatically pressed nuclear graphite BG80, which is widely used in HTGRs, as the research object, and designed and constructed a graphite friction coefficient testing apparatus capable of simulating the core environment. The apparatus adopted an end face contact configuration of a graphite rod against a graphite rod, driven by a servo motor and loaded by a bellows. It can accurately acquire the driving force and rebound force–displacement curves under a temperature range of 25–1300 °C, a load range of 0–30 kg (corresponding to a contact surface pressure of about 31.25–68.75 kPa, close to the actual stress level of core graphite components), and under different atmospheres (high purity helium/nitrogen) [88].

In terms of data processing, a systematic and rigorous methodology was adopted: first, the system resistance was determined based on the non-return condition of the graphite test pieces, and it was found that this system resistance was only related to the characteristics of the apparatus itself and not affected by external factors such as temperature, atmosphere, and load. Then, by analyzing the rebound force data, a fitting relationship between the bellows elastic force and displacement was established, thereby verifying the stability of the elastic force throughout the test process. Finally, by combining the system resistance and the elastic force to correct the driving force data, the average friction force curves under various working

conditions were obtained [88]. A total of 4 test groups were completed in a helium atmosphere and 2 groups in a nitrogen atmosphere, covering the complete temperature range from room temperature to 1300 °C, which fully encompasses the temperature range under normal HTGR operation and some accident conditions [89].

The experimentally obtained static and dynamic friction coefficients between graphite were as follows [90]: in a helium atmosphere (Figure 14), the maximum static friction coefficient was 0.20856 (low temperature range) and the minimum was 0.03796 (high-temperature range); the maximum average dynamic friction coefficient was 0.17852, and the minimum was 0.03942. In a nitrogen atmosphere, the maximum static friction coefficient was 0.25550, and the minimum was 0.04225; the maximum dynamic friction coefficient was 0.23190, and the minimum was 0.03293 [6]. The dynamic friction coefficient did not change significantly with sliding displacement, indicating that within the load range of this test (without reaching plastic deformation of graphite), the friction coefficient was essentially independent of load and displacement [91].

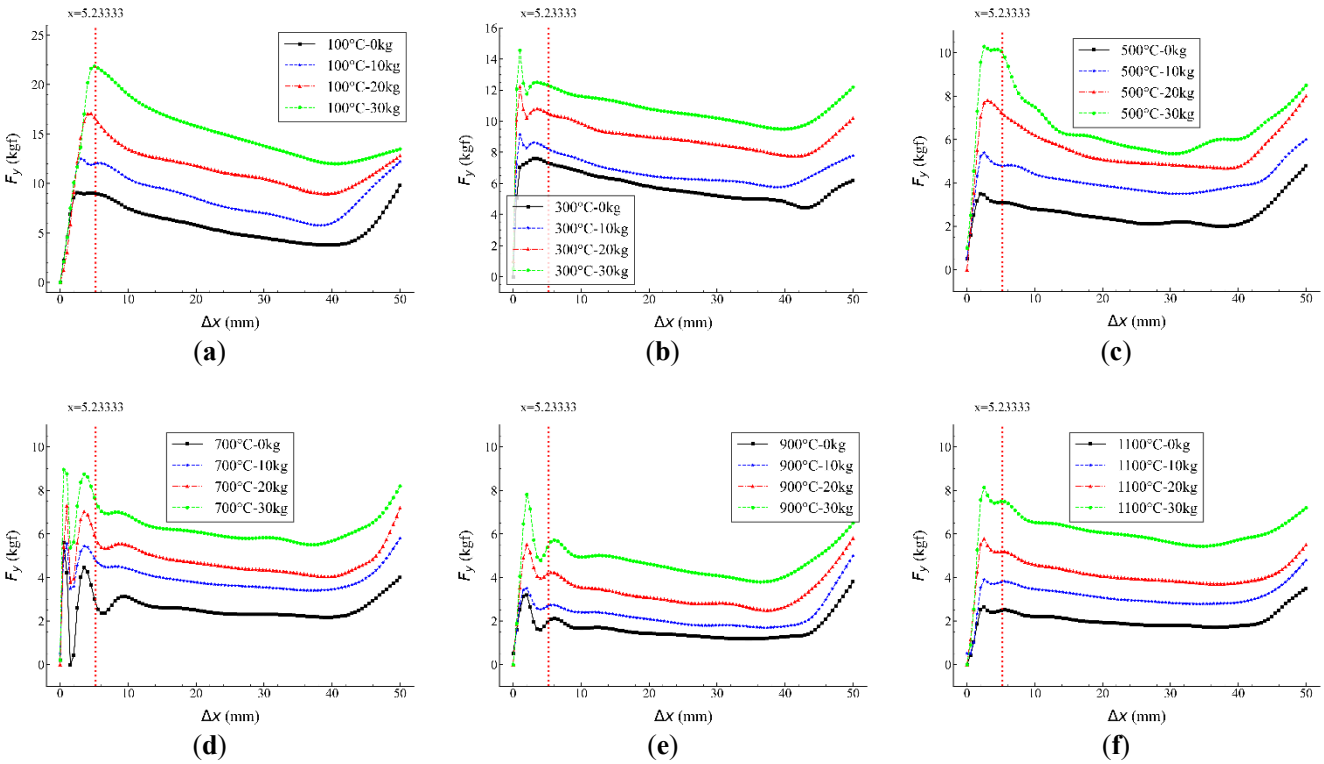

Figure 14. Friction coefficient measurement at different temperatures in helium ((**a**). 100 °C; (**b**). 300 °C, (**c**). 500 °C; (**d**). 700 °C; (**e**). 900 °C, (**f**). 1100 °C).

The variation of the friction coefficient with temperature exhibited a clear four stage characteristic [91]:

(I) Room temperature to about 200 °C: The friction coefficients in both atmospheres increased with increasing temperature. During this stage, water and oxygen molecules adsorbed on the graphite friction surface gradually desorbed, and the lubricating adsorbed film collapsed, thereby increasing the friction coefficient. The friction coefficient in nitrogen was significantly higher than that in helium, because helium atoms have a small radius and could already intercalate between graphite layers to provide lubrication, whereas nitrogen molecules faced more difficulty.

(II) 200 °C to about 400 °C: After the complete failure of the adsorbed film, the friction coefficient decreased with increasing temperature. The increase in temperature enlarged the graphite interlayer

spacing, increasing the opportunity for gas atoms to intercalate between the layers and making microsliding between graphite crystals easier.

(III) 400 °C to about 900 °C: The friction coefficient entered a relatively stable plateau, varying gently with temperature. At this stage, the effects of interlayer spacing increase, and gas intercalation has reached a quasi-equilibrium state.

(IV) 900 °C to 1300 °C: The dynamic friction coefficient increased slightly with increasing temperature. At high temperatures, the graphite friction surface was more prone to exfoliation, and the number of generated fine graphite particles increased, with the mechanical hindrance effect on relative sliding gradually becoming apparent.

At temperatures above about 300 °C, since nitrogen molecules could also enter the graphite interlayer space, the friction coefficients in the two atmospheres tended to converge [92]. The above findings provide the first set of quantitative friction data under continuous temperature variation for pebble bed flow calculations and fuel handling system design in HTGRs.

6.1.2. The Uncertainty Analysis

The uncertainty in experimental results can be categorized as Type A and Type B uncertainties. Type A uncertainty is evaluated through statistical analysis of the experimental data, typically using the Bessel method. In this study, the best estimate of the friction coefficient μ is represented by the mean value of n independent measurements. The standard uncertainty, expressed as the standard deviation, quantifies the dispersion of the measurement results. Accordingly, the standard uncertainty $u(\mu_k)$ of any individual measurement μ_k is given by the experimental standard deviation $s(\mu_k)$, calculated using the Bessel formula. For practical measurements, the Type A uncertainty of the best estimate as follows

$$u(\mu_k) = s(\mu_k) = \sqrt{\frac{1}{n-1}\sum_{k=1}^{n}(\mu_k - \bar{\mu})^2},\ u_A(\bar{\mu}) = s(\bar{\mu}) = \sqrt{\frac{1}{n(n-1)}\sum_{k=1}^{n}(\mu_k - \bar{\mu})^2} \tag{1}$$

Type A uncertainty is obtained solely from the statistical evaluation of measurement results. In contrast, Type B uncertainty can originate from various sources, such as calibration certificates, instrument specifications, technical documentation, prior data, or expert experience.

In the present study, the friction coefficient μ is calculated from the measured friction force and normal load. Therefore, the Type B uncertainty is primarily determined by the uncertainties of the force-measuring instruments and the calibration weights used for loading, as listed in Table 4. The standard Type B uncertainty of an input quantity $u_B(x)$ is determined by the absolute value of its error limit a and a divisor factor, which is typically taken as $\sqrt{3}$ for a rectangular distribution $u_B(x) = \frac{a}{\sqrt{3}}$.

The Type B uncertainty of the mean value $u_B(\bar{\mu})$ is calculated as:

$$\frac{u_B(\bar{\mu})}{\bar{\mu}} = \frac{1}{\bar{\mu}}\sqrt{u_B(\bar{F}_f) + u_B(\bar{N})} = \sqrt{6\left(\frac{0.005\%}{\sqrt{3}}\right)^2 + \left(\frac{0.3\%}{\sqrt{3}}\right)^2 + \left(\frac{0.005\%}{\sqrt{3}}\right)^2} = 0.17337339\% \tag{2}$$

The uncertainties are evaluated for all friction coefficient results presented here. For other measured quantities, such as the bellows elastic force F_e and system resistance F_r,

$$\begin{cases} F_{push} = F_e + F_f - F_r \text{ (during push forward)} \\ F_{pull} = F_e - F_r \text{ (during pull back)} \end{cases} \tag{3}$$

the uncertainty calculation differs slightly. While the Type A uncertainty remains applicable according to Equation (1), the Type B uncertainty excludes the contribution from the calibration weights, as these

quantities are independent of the applied load. Consequently, Type B uncertainty of system resistance is computed by:

$$\frac{u_B(\bar{F}_r)}{\bar{F}_r} = \sqrt{\left(\frac{0.3\%}{\sqrt{3}}\right)^2 + \left(\frac{0.005\%}{\sqrt{3}}\right)^2} = 0.17322914\% \tag{4}$$

The combined standard uncertainty $u_C(\bar{\mu})$ of the mean $\bar{\mu}$ is then obtained from the law of uncertainty propagation $u_C(\bar{\mu}) = \sqrt{u_A^2(\bar{\mu}) + u_B^2(\bar{\mu})}$.

Table 4. Instruments and equipment involved in Type B uncertainty evaluation.

Instrument/Equipment	Quantity	Relative Accuracy
Calibration weights	6	±0.005%
Cylindrical load cell	1	±0.3%
Pressure transmitter digital indicator	1	±0.005%

6.1.3. Mechanism Interpretation of the Effects of Temperatures and Atmospheres

The static and kinetic friction coefficients exhibit very similar temperature dependent behavior, generally showing an initial increase followed by a decrease and then stabilization. Specifically: below 200 °C, the friction coefficient increases slightly with rising temperature, reaching a maximum around 200 °C; above 200 °C, the friction coefficient decreases significantly with further temperature increase, and stabilizes after 400 °C; when the temperature continues to rise above 900 °C, the kinetic friction coefficient shows a slight increase.

The mechanisms for the effects of temperature on the friction might be interpreted as follows:

(1) For the rising stage below 200 °C: at lower temperatures, the graphite friction surface is covered by a physical or chemical adsorbed layer (e.g., water vapor or air molecules) that provides a certain lubricating effect. As temperature increases, this adsorbed layer gradually desorbs or disintegrates, exposing the originally passivated active surface and generating more "dangling bonds," which enhance interfacial adhesion and consequently increase the friction coefficient, reaching a peak around 200 °C.

(2) For the declining stage from 200 °C to 400 °C: when the temperature exceeds 200 °C, the friction coefficient drops rapidly, owing to the synergistic effects of multiple mechanisms: (a). Thermally assisted interlayer insertion: rising temperature increases the interlayer spacing of the graphite crystal lattice, while gas molecules (atoms) become more energetic. In a helium (He) atmosphere, the smaller He atoms can more readily insert themselves between the graphite layers, weakening the interlayer van der Waals forces and reducing the interlayer shear strength. (b). The thermal passivation of active sites: the thermal energy provided by elevated temperatures promotes the rearrangement or exfoliation of graphite microcrystallites. These processes effectively cover or saturate the highly reactive "dangling bonds" at the friction interface, thereby reducing the adhesive contribution to friction. (c). Contact mechanics effects: From the perspective of rough surface contact, higher temperatures may lead to a reduction in the real contact area or promote the formation of a more stable transfer film, thereby lowering frictional resistance.

(3) Beyond 400 °C, the insertion and passivation effects approach saturation, and the friction coefficient enters a stable low value plateau.

(4) slight increase above 900 °C: when the temperature rises above 900 °C, the amount of wear debris or fine graphite particles exfoliated from the friction surface increases. The rolling or accumulation of

these particles at the interface may intensify ploughing effects or hinder smooth sliding, leading to a slight increase in the friction coefficient.

Comparing the friction results in helium (He) and nitrogen (N_2), the mechanism of the influence of the environmental atmosphere is interpreted as follows:

(1) below 200 °C: The effect of the atmosphere is highly significant. The friction coefficient of graphite in a N_2 atmosphere is markedly higher than that in a He atmosphere. The fundamental reason lies in the difference in intercalation at the atomic scale: He atoms (kinetic diameter ~0.26 nm) are much smaller than N_2 molecules (kinetic diameter ~0.36 nm), enabling them to more effectively insert themselves between the graphite layers even at lower temperatures, acting as "ball bearings" or "spacers" that lubricate and more effectively reduce the friction coefficient.

(2) above 200 °C (especially above 300 °C): As the temperature rises, the interlayer spacing of the graphite lattice further expands due to thermal expansion, while the kinetic energy of gas molecules increases significantly. Under these conditions, even the slightly larger N_2 molecules can overcome the energy barrier and enter the graphite interlayer spaces. Consequently, at elevated temperatures (e.g., above 400 °C), the friction coefficients of graphite in He and N_2 atmospheres become very close, and the lubricating effects of the two gases tend to converge.

Based on the high similarity in friction behavior between N_2 and He atmospheres at elevated temperatures (above 300 °C), it is feasible to use nitrogen (N_2) as a substitute for expensive helium (He) as the working gas in exploratory or validation experiments related to high temperature gas cooled reactor cores. This substitution effectively simulates the tribological behavior of graphite components in the reactor core while significantly reducing experimental costs, offering favorable economic benefits for engineering design and innovative validation.

6.2. Experimental Study on the Stiffness Coefficient of Fuel Pebbles in High Temperature Helium

The second study focused on the stiffness coefficient of spherical fuel elements. An experimental system consisting of a graphite sphere in compressive contact with a graphite rod was established, and the load–displacement response of the fuel sphere was measured at different temperatures in a high temperature helium environment [2]. For theoretical modeling, the fuel sphere contact problem was decomposed into two cases: graphite sphere-on-sphere contact and graphite sphere-on-rod contact. For the former, the Hertz contact theory was used to derive the relationship between deformation and external load; for the latter, the method of dimensionality reduction was employed to establish an analytical force–displacement relationship, and the correctness of the theoretical model was verified by finite element numerical simulation [92]. Finally, a relational expression linking the directly measured quantity in the experiment (the overall system displacement) with the stiffness coefficient of the fuel sphere itself was derived, enabling the accurate extraction of material parameters from the experimental data.

The experiments revealed an important characteristic of the temperature dependence of the fuel sphere stiffness coefficient: it exhibited unidirectional irreversibility. When the temperature was increased from room temperature to a high temperature and then decreased back to the initial temperature, the stiffness coefficient did not return to its original value, demonstrating a significant dependence on thermal history [92]. This phenomenon is attributed to two kinds of mechanisms: (1). The intrinsic elastic modulus of graphite tends to increase with temperature, the interplay between modulus evolution, residual stress relaxation, and microstructural characteristics profoundly dictates the resultant macroscopic rigidity and failure behavior. In coarse-grained Gilsocarbon graphite [93], the dominant stress relaxation and extensive extrinsic toughening promote a more compliant, damage-tolerant response with enhanced failure strains at high temperatures. Conversely, in fine-grained graphites [94], the disproportionate increase in modulus

relative to strength, coupled with limited residual stress relief and scarce toughening mechanisms, renders the material stiffer yet more brittle, with reduced failure strains and a marked propensity for catastrophic fracture. (2). Irreversible closure and structural adjustment of microcracks (such as Mrozowski cracks) inside the graphite during thermal cycling, which has important implications for understanding the mechanical behavior evolution of fuel spheres under long term operational thermal cycling. These behaviors underscore that the temperature-dependent rigidity of nuclear graphite cannot be inferred solely from modulus measurements, but must be understood within the broader context of residual stress states, microstructural heterogeneity, and the prevailing toughening mechanisms that collectively dictate the material's structural integrity under high-temperature reactor operating conditions. In addition, the study used various functional forms, including polynomial and exponential functions, to fit the stiffness coefficient–temperature relationship, yielding concise analytical expressions with recommended ranges of applicability for engineering convenience [2].

The recent work carried out by Si et al. [95] fills the experimental gap in the contact stiffness coefficient of spherical fuel elements in a high temperature helium environment and provides crucial input parameters for fuel element design and core deformation simulations (Figure 15).

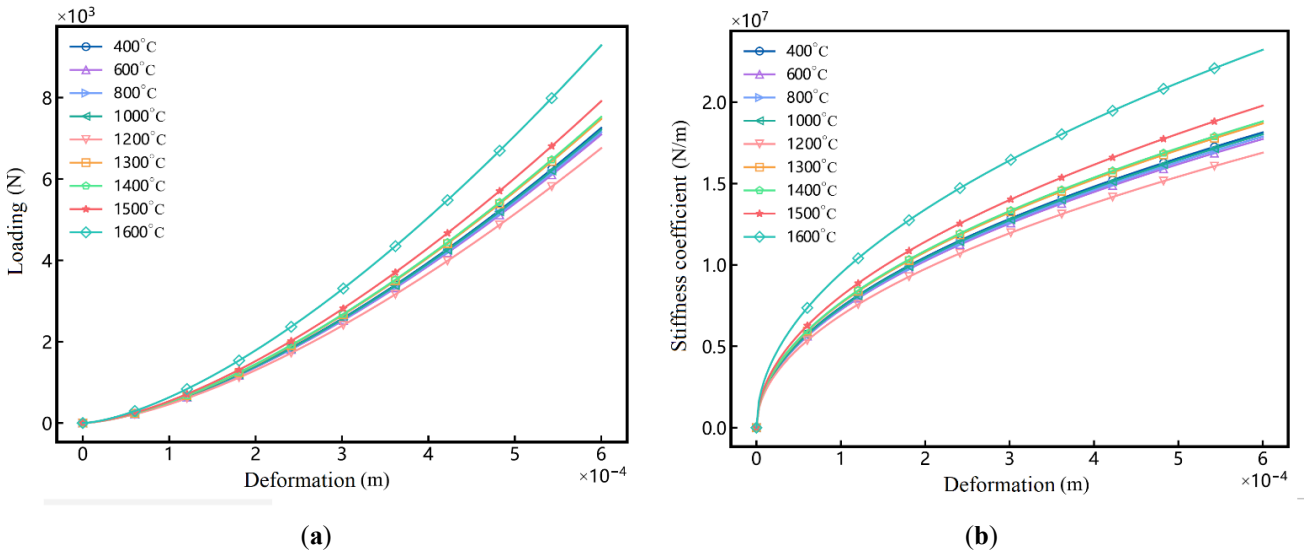

Figure 15. The measurement results of relationships between loading deformation (**a**) and stiffness coefficient deformation (**b**) at various temperatures in helium.

7. Recommendations for Future Work

Along with the current state of research on the friction and stiffness of graphite, the following aspects are suggested for future investigation:

(1) Experimental measurement of the friction and stiffness of graphite after irradiation. Such data are essential for evaluating the mechanical integrity and reliability of graphite materials used in pebble-bed reactors. Potentially, these measurements could be performed on pebbles discharged from operational reactors, such as HTR-10 or the HTR-PM power plant. It is preferable to use non-fuel graphite pebbles rather than spent fuel pebbles, so as to avoid complications arising from radioactivity and fuel handling.

(2) Measurement of the equivalent stiffness of a small-scale pebble bed under high-temperature helium atmosphere. Although measurements of pebble-cluster stiffness have been carried out, they have been limited to linear packing configurations, which differ from the actual packing structure in a real pebble bed. It is therefore more pertinent to determine the equivalent stiffness of a packed pebble bed, in order

to clarify the coupling between single-pebble stiffness and local void fraction, as well as their combined influence on pebble flowability and residence time distribution within the bed.

(3) Determination of the rolling friction coefficient of spherical pebbles under high-temperature helium conditions. Previous friction-coefficient measurements in high-temperature helium have focused on sliding friction rather than rolling friction. Given that pebbles in a reactor bed undergo rolling motion during operation, it is advisable to perform direct measurements of the rolling friction coefficient using actual spherical pebbles under relevant high-temperature helium environments.

8. Conclusions and Outlook

The friction coefficient and contact stiffness of nuclear graphite materials in HTGRs are indispensable fundamental parameters for core mechanical design, pebble bed flow path analysis, and safety assessments. Based on a systematic review of the characteristics of nuclear graphite materials and the current status of tribology and contact mechanics research, this paper integrates the results of the two latest systematic experimental studies, with the main conclusions as follows:

(1) The friction behavior of nuclear graphite is jointly controlled by the ambient atmosphere and temperature. In a high purity helium atmosphere, as the temperature increases, the friction coefficient of graphite undergoes an ascending stage controlled by the adsorbed film (room temperature–200 °C), a descending stage dominated by interlayer spacing increase and gas intercalation effects (200–400 °C), a quasi-equilibrium stable stage (400–900 °C), and a slight ascending stage caused by particle exfoliation (900–1300 °C). The overall pattern exhibits a complex trend of first increasing, then decreasing, then stabilizing, and finally slightly increasing. In the low temperature range, helium provides better lubrication than nitrogen due to its atomic size effect, resulting in a lower friction coefficient; at high temperatures, the friction coefficients in the two atmospheres tend to converge.

(2) The contact stiffness coefficient of spherical fuel elements in high temperature helium exhibits significant temperature dependence and irreversible evolution characteristics. The irreversible closure of microcracks during the heating process leads to a thermal history effect on the stiffness coefficient, a finding that has important implications for the lifetime behavior assessment of fuel elements.

(3) Existing research still has prominent shortcomings, including a data gap in the irradiation–thermal–mechanical coupling of nuclear graphite, fractal contact models not yet characterized for graphite specific microstructural features, and the lack of a unified theoretical framework for friction and stiffness.

(4) Future research should focus on advancing the following directions: conducting experiments on the friction and contact stiffness of irradiated nuclear graphite in high temperature environments to clarify the coupling effects between irradiation damage and interface mechanics; establishing an interface contact model that considers the multiscale microstructure of nuclear graphite (grains, Mrozowski cracks, pores, *etc.*) and the fractal rough surface features, and docking it with pebble bed discrete element simulations or whole-core finite element analysis; and developing a unified interface mechanics characterization system for the friction coefficient and contact stiffness, achieving multiscale bridging from microscopic mechanisms to macroscopic core behavior, thereby providing solid support for the refined design and long term safety evaluation of HTGRs.

Acknowledgments

The authors are grateful for the support of this research by the LingChuang Research Project of China National Nuclear Corporation (Recipient : Qian Wang).

Author Contributions

Conceptualization, T.L.; Methodology, M.S. and Z.C.; Writing—Original Draft Preparation, T.L.; Supervision, N.G.; Project Administration, S.J.

Ethics Statement

Not applicable.

Informed Consent Statement

Not applicable.

Data Availability Statement

Data will be available from the corresponding author on request.

Funding

This research was funded by [National Major Science and Technology Program, and LingChuang Research Project of China National Nuclear Corporation].

Declaration of Competing Interest

The authors declare that they have no known competing financial interests or personal relationships that could have appeared to influence the work reported in this paper.

References

1. Available online: https://www.gov.cn/zhengce/zhengceku/2022-04/03/content_5683361.htm (accessed on 29 November 2021).
2. Abram T, Ion S. Generation-IV nuclear power: A review of the state of the science. *Energy Policy* **2008**, *36*, 4323–4330. DOI:10.1016/j.enpol.2008.09.059
3. Chen F, Dong Y, Zheng Y, Shi L, Li F, Zhang Z. Progress of the HTR-10 measured data utilization. In Proceedings of the 2014 International Conference on Nuclear Engineering, New York, NY, USA, 7–11 July 2014; V003T05A003.
4. Sears VF. Neutron scattering lengths and cross sections. *Neutron News* **1992**, *3*, 26–37. DOI:10.1080/10448639208218770
5. Lin LP, Lin JF. An elastoplastic microasperity contact model for metallic materials. *J. Tribol.* **2005**, *127*, 666–672. DOI:10.1115/1.1843830
6. Gao LB, Shen J. *The Development and Perspective of HTGR*; China Nuclear Industry: Beijing, China, 2016; pp. 24–27.
7. Zhang Z, Wu Z, Wang D, Xu Y, Sun Y, Li F, et al. Current status and technical description of Chinese 2 x 250 MWth HTR-PM demonstration plant. *Nucl. Eng. Des.* **2009**, *239*, 1212–1219. DOI:10.1016/j.nucengdes.2009.02.023
8. Zhou XW, Yang Y, Song J, Lu ZM, Zhang J, Liu B, et al. Carbon materials in a high temperature gas-cooled reactor pebble-bed module. *New Carbon Mater.* **2018**, *33*, 97–108. DOI:10.1016/S1872-5805(18)60328-2
9. Marsden BJ, Jones AN, Hall GN, Treifi M, Mummery PM. Graphite as a core material for Generation IV nuclear reactors. In *Structural Materials for Generation IV Nuclear Reactors*; Elsevier: Amsterdam, The Netherlands, 2017; pp. 495–532.
10. Luo XW, Yu SY, Zhang ZS, He SY. Estimation of Graphite Dust Quantity and Size Distribution of Graphite Particle in HTR-10. *Nucl. Power Eng.* **2005**, *26*, 203–208. Available online: https://inis.iaea.org/records/p6rhp-yr494 (accessed on 16 August 2025).
11. Rycroft CH, Grest GS, Landry JW, Bazant MZ. Analysis of granular flow in a pebble-bed nuclear reactor. *Phys. Rev. E* **2006**, *74*, 21306. DOI:10.1103/PhysRevE.74.021306
12. Hennings U. Fuel Handling System For Core Elements Of a Pebble-Bed Reactor. *Nucl. Appl. Technol.* **1969**, *7*, 334–341. DOI:10.13182/NT69-A28475
13. Xu SJ, Kang FY. *Carbon and Graphite Materials in Nuclear Engineering*; Tsinghua University Press: Beijing, China, 2011.

14. Zhang Z, Dong Y, Li F, Zhang Z, Wang H, Huang X, et al. The Shandong Shidao Bay 200 MWe High-Temperature Gas-Cooled Reactor Pebble-Bed Module (HTR-PM) Demonstration Power Plant: An Engineering and Technological Innovation. *Engineering* **2016**, *2*, 112–118. DOI:10.1016/J.ENG.2016.01.020
15. Bacon G. A method for determining the degree of orientation of graphite. *J. Appl. Chem.* **1956**, *6*, 477–481. DOI:10.1002/jctb.5010061101
16. Shen K, Yu S, Kang F. The microstructure and texture of Gilsocarbon graphite. *Carbon* **2019**, *153*, 428–437. DOI:10.1016/j.carbon.2019.06.108
17. Mnozot'sxr S. Mechanical Strength, Thermal Expansion and Structure of Cokes and Carbons. 1956. Available online: https://personal.ems.psu.edu/~radovic/1953/papers/1953_31.PDF (accessed on 16 August 2026).
18. Wang P. The Oxidation Performance of IG-110 Nuclear Graphite Used in HTGRs. Ph.D. Thesis, Tsinghua University, Beijing, China, 2013.
19. Nabielek H, Kaiser G, Huschka H, Ragoss H, Wimmers M, Theymann W. Fuel for pebble-bed HTRs. *Nucl. Eng. Des.* **1984**, *78*, 155–166. DOI:10.1016/0029-5493(84)90301-7
20. Ivens G, Wimmers M. The AVR as a test bed for fuel elements. In *The AVR Reactor-Twenty Years of Operation*; VDI-Verlag: Düsseldorf, Germany, 1989.
21. Hertz H. On the contact of solid elastic bodies and on hardness. *J. Math.* **1881**, *92*, 156–171. DOI: 10.1515/crll.1882.92.156
22. Tabor D. *The Hardness of Metals*; Oxford University Press: Oxford, UK, 2000.
23. Jenkins GM. Analysis of the stress-strain relationships in reactor grade graphite. *Br. J. Appl. Phys.* **1962**, *13*, 30. DOI:10.1088/0508-3443/13/1/307
24. Zhou Q, Xu RQ. The Lubricating Properties of Graphite Materials and Their Development and Applications. *New Carbon Mater.* **1997**, 13–18. Available online: https://www.cnki.com.cn/Journal/B-B2-XTCL-1997-03.htm (accessed on 16 August 2026).
25. Luo XW, Yu SY, Sheng XY, He SY, Zhang ZS. Friction Property of Chinese Graphite Used in High Temperature Gas-cooled Reactor. *Nucl. Power Eng.* **2001**, *22*, 318–320. Available online: https://inis.iaea.org/records/xjc9w-dmd25 (accessed on 16 August 2026).
26. Luo XW, Yu SY, Sheng XY, He SY, Zhang ZS. Tribological Properties Differences of Various Graphite Used in 10 MW High Temperature Gas-cooled Reactor. *At. Energy Sci. Technol.* **2004**, *38*, 226–230. Available online: https://inis.iaea.org/records/3rspb-f0r32 (accessed on 16 August 2026).
27. Zhu ZG, Wang S, Ren Y, Wang TB, Bai S, Wu JF. Friction and wear behavior of carbon graphite materials in mechanical seal. *Carbon Tech.* **2017**, *36*, 34–37. Available online: https://tsjs.cbpt.cnki.net/portal/journal/portal/client/paper/380d9621e0d61868f291a8aaaf7c3379 (accessed on 16 August 2026).
28. Xu YX. Structural Design and Mechanical and Tribological Properties of Carbon-Graphite Materials for Machinery. Ph.D. Thesis, Hunan University, Changsha, China, 2022.
29. Skinner J, Gane N, Tabor D. Micro-friction of Graphite. *Nat. Phys. Sci.* **1971**, *232*, 195–196. DOI:10.1038/physci232195a0
30. Liu B, Zhao H, Li X, Yang Z, Zhang D, Liu Z. Effect of pore structure on the thermophysical and frictional properties of high-density graphite. *Micropor. Mesopor. Mater.* **2022**, *330*, 111613. DOI:10.1016/j.micromeso.2021.111613
31. Li XN, Zhou XW, Lu ZM, Zhang J, Liu B. Current status and future prospect of researches on the frictional properties of graphite for high temperature gas-cooled reactor. *Carbon Tech.* **2014**, *33*, 28–31. DOI:10.14078/j.cnki.1001-3741.2014.06.008.
32. Zaidi H, Robert F, Paulmier D. Influence of adsorbed gases on the surface energy of graphite: consequences on the friction behaviour. *Thin Solid Film.* **1995**, *264*, 46–51. DOI:10.1016/0040-6090(95)06606-3
33. Paulmier D, Zaidi H. The friction coefficient of hydrogenated surfaces of polycrystalline graphite. *Vacuum* **1990**, *41*, 1314–1316. DOI:10.1016/0042-207X(90)93944-E
34. Savage RH. Graphite Lubrication. *J. Appl. Phys.* **1948**, *19*, 1–10. DOI:10.1063/1.1697867
35. Spreadborough J. The frictional behaviour of graphite. *Wear* **1962**, *5*, 18–30. DOI:10.1016/0043-1648(62)90177-1
36. Xiao J, Zhang L, Zhou K, Li J, Xie X, Li Z. Anisotropic friction behaviour of highly oriented pyrolytic graphite. *Carbon* **2013**, *65*, 53–62. DOI:10.1016/j.carbon.2013.07.101
37. Rietsch JC, Brender P, Dentzer J, Gadiou R, Vidal L, Vix-Guterl C. Evidence of water chemisorption during graphite friction under moist conditions. *Carbon* **2013**, *55*, 90–97. DOI:10.1016/j.carbon.2012.12.013
38. Luo XW, Yu SY, Sheng XY, He SY, Zhang ZS. Friction Performance of Three Kinds of Graphite Used in Nuclear Reactors. *Chin. High Technol. Lett.* **2001**, *11*, 97–100.

39. Kumar N, Dash S, Tyagi AK, Raj B. Super low to high friction of turbostratic graphite under various atmospheric test conditions. *Tribol. Int.* **2011**, *44*, 1969–1978. DOI:10.1016/j.triboint.2011.08.012
40. Wild E, Mack KJ. Lubrication of nuclear reactor components Friction systems in liquid sodium and argon. *Tribol. Int.* **1978**, *11*, 321–324. DOI:10.1016/0301-679X(78)90037-3
41. Rowe GW. The friction and strength of clean graphite at high temperatures. *Wear* **1960**, *3*, 454–462. DOI:10.1016/0043-1648(60)90229-5
42. Semenov AP. Tribology at high temperatures. *Tribol. Int.* **1995**, *28*, 45–50. DOI:10.1016/0301-679X(95)99493-5
43. Driesner AR, Wagner P. Friction Coefficients of Graphite over the Temperature Interval 25 °C to 2450 °C. *J. Appl. Phys.* **1958**, *29*, 901–903. DOI:10.1063/1.1723326
44. Lancaster JK, Pritchard JR. The influence of environment and pressure on the transition to dusting wear of graphite. *J. Phys. D Appl. Phys.* **1981**, *14*, 747–762. DOI:10.1088/0022-3727/14/4/027
45. Luo XW, Yu SY, Sheng XY, He SY, Zhang ZS. Effect of Temperatures on the Friction Behavior of Graphite Used in a Nuclear Reactor. *Tribology* **2004**, *24*, 402–405. Available online: https://www.researchgate.net/publication/289187852_Effect_of_temperatures_on_the_friction_behavior_of_graphite_used_in_a_nuclear_reactor (accessed on 16 August 2026).
46. Luo XW. Research on Graphite Dust Behavior in 10MW High Temperature Gas-Cooled Reactor. Ph.D. Thesis, Tsinghua University, Bejing, China, 2004.
47. Fu ZQ, Tang CH, Liang TX, Li ZQ. Influence of SiC Coatings on the Tribological Behaviors of Graphite for High Temperature Gas-Cooled Reactor. *Heat Treat. Met.* **2005**, *30*, 13–16. Available online: https://www.researchgate.net/publication/292687826_Influence_of_SiC_coatings_on_the_tribological_behaviors_of_graphite_for_high_temperature_gas-cooled_reactor (accessed on 16 August 2026).
48. Kumar N, Kozakov AT, Ravindran TR, et al. Load dependent friction coefficient of crystalline graphite and anomalous behavior of wear dimension. *Tribol. Int*. **2015**, *88*, 280–289. DOI:10.1016/j.triboint.2015.03.034
49. Li XN, Zhou XW, Lu ZM, Zhang J, Liu B. Friction and wear properties of matrix graphite in spherical fuel element for HTR. *Carbon Tech.* **2016**, *35*, 1–6. Available online: https://www.researchgate.net/publication/303274210_Friction_and_wear_properties_of_matrix_graphite_in_spherical_fuel_element_for_HTR (accessed on 16 August 2026).
50. Csapo E, Zaidi H, Paulmier D. Friction behaviour of a graphite-graphite dynamic electric contact in the presence of argon. *Wear* **1996**, *192*, 151–156. DOI:10.1016/0043-1648(95)06788-4
51. Lancaster JK. Transitions in the Friction and Wear of Carbons and Graphites Sliding Against Themselves. *ASLE Trans.* **1975**, *18*, 187–201. DOI:10.1080/05698197508982761
52. Abbott EJ, Firestone FA. Specifying surface quality a method based on accurate measurement and comparison. *Mech. Eng.* **1933**, *55*, 569–572. Available online: https://archive.org/details/sim_mechanical-engineering_1933-09_55_9/page/569/mode/1up (accessed on 16 August 2026).
53. Chang W, Etsion I, Bogy DB. An elastic-plastic model for the contact of rough surfaces. *J. Tribol.* **1987**, *109*, 257–263. DOI:10.1115/1.3261348
54. Zhao Y, Maietta DM, Chang L. An asperity microcontact model incorporating the transition from elastic deformation to fully plastic flow. *J. Tribol.* **2000**, *122*, 86–93. DOI:10.1115/1.555332
55. Xiao H, Sun Y, Chen Z. Fractal modeling of normal contact stiffness for rough surface contact considering the elastic–plastic deformation. *J. Braz. Soc. Mech. Sci. Eng.* **2019**, *41*, 1–13. DOI:10.1007/s40430-018-1513-x
56. Kogut L, Etsion I. Elastic-plastic contact analysis of a sphere and a rigid flat. *J. Appl. Mech.* **2002**, *69*, 657–662. DOI:10.1115/1.1490373
57. Jackson RL, Green I. A statistical model of elasto-plastic asperity contact between rough surfaces. *Tribol. Int.* **2006**, *39*, 906–914. DOI:10.1016/j.triboint.2005.09.001
58. Popov VL. *Contact Mechanics and Friction Phyiscal Principles and Application*; Tsinghua University Press: Beijing, China, 2011.
59. Greenwood JA, Williamson JP. Contact of nominally flat surfaces. *Proc. R. Soc. Lond. A* **1966**, *295*, 300–319. DOI:10.1098/rspa.1966.0242
60. Majumdar A, Tien C. Fractal characterization and simulation of rough surfaces. *Wear* **1990**, *136*, 313–327. DOI:10.1016/0043-1648(90)90154-3
61. Majumdar A, Bhushan B. Role of fractal geometry in roughness characterization and contact mechanics of surfaces. *J. Tribol.* **1990**, *112*, 205–216. DOI:10.1115/1.2920243

62. Wang S, Komvopoulos K. A fractal theory of the temperature distribution at elastic contacts of fast sliding surfaces. *J. Tribol.* **1995**, *117*, 203–215. DOI:10.1115/1.2831227
63. Yan W, Komvopoulos K. Three-dimensional fractal analysis of rough surfaces. *J. Appl. Phys.* **1998**, *84*, 3617–3624. DOI:10.1063/1.368536
64. Zhao Y, Fang C, Cai L, Liu Z. A three-dimensional fractal theory based on thermal contact conductance model of rough surfaces. *Proc. Inst. Mech. Eng. Part E J. Process Mech. Eng.* **2018**, *232*, 528–539. DOI:10.1177/0954408917727198
65. Thomas T, Sayles R. Stiffness of machine tool joints: a random-process approach. *J. Eng. Ind.* **1977**, *99*, 250–256. DOI:10.1115/1.3439147
66. Yuan B, Sun Q, Wang X, Mu X, Wang Y, Sun W. A novel acoustic model for interface stiffness measurement of dry tribological interface considering geometric dispersion effect and boundary effect. *Tribol. Int.* **2021**, *162*, 107140. DOI:10.1016/j.triboint.2021.107140
67. Wang J, Horng S. Investigation of the tool holder system with a taper angle 7:24. *Int. J. Mach. Tools Manuf.* **1994**, *34*, 1163–1176. DOI:10.1016/0890-6955(94)90020-5
68. Krolikowski J, Szczepek J. Prediction of contact parameters using ultrasonic method. *Wear* **1991**, *148*, 181–195. DOI:10.1016/0043-1648(91)90216-H
69. Dwyer-Joyce R. The application of ultrasonic NDT techniques in tribology. *Proc. Inst. Mech. Eng. Part J J. Eng. Tribol.* **2005**, *219*, 347–366. DOI:10.1243/135065005X9763
70. Jia S, Yi Y, Wang L, Liu G, Ma Q, Sun L, et al. Study on failure mechanism of line contact structures of nuclear graphite. *Nucl. Eng. Technol.* **2022**, *54*, 2989–2998. DOI:10.1016/j.net.2022.03.018
71. Zou Z, Fok SL, Oyadiji SO, Marsden BJ. Failure predictions for nuclear graphite using a continuum damage mechanics model. *J. Nucl. Mater.* **2004**, *324*, 116–124. DOI:10.1016/j.jnucmat.2003.09.005
72. Yang X, Gao Y, Zhong Y, Ding D, Tsang DKL. Stress analysis of the TMSR graphite component under irradiation conditions. *Nucl. Sci. Tech.* **2018**, *29*, 173. DOI:10.1007/s41365-018-0516-8
73. Song W, Li KM, Ma RR, Li WJ, Ding XX, Chen HX. Study on Wear Properties of Impregnated Graphite Materials under Different Normal Loads. *Lubr. Eng.* **2023**, 1–10.
74. Xu YX, Tan J, Tu CJ, Liang SL, Yin JF, Xiong W, et al. Effect of temperature and load changes on friction and wear properties of carbon graphite materials for sealing. *Carbon* **2021**, *1*, 3–10. DOI: 10.3969/j.issn1001-8948.2021-01-001
75. Aranganathan N, Bijwe J. Comparative performance evaluation of NAO friction materials containing natural graphite and thermo-graphite. *Wear* **2016**, *358–359*, 17–22. DOI:10.1016/j.wear.2016.03.032
76. Bowden FP, Young JE. Friction of diamond, graphite, and carbon and the influence of surface films. *Proc. R. Soc. London. Ser. A Math. Phys. Sci.* **1951**, *208*, 444–455. DOI:10.1098/rspa.1951.0173
77. Jin H, Zhou K, Ji Z, Tian X, Chen Y, Lu L, et al. Comparative tribological behavior of friction composites containing natural graphite and expanded graphite. *Friction* **2020**, *8*, 684–694. DOI:10.1007/s40544-019-0293-3
78. Lancaster JK, Pritchard JR. On the 'dusting' wear regime of graphite sliding against carbon. *J. Physics. D Appl. Phys.* **1980**, *13*, 1551–1564. DOI:10.1088/0022-3727/13/8/025
79. Morstein CE, Dienwiebel M. Graphite lubrication mechanisms under high mechanical load. *Wear* **2021**, *477*, 203794. DOI:10.1016/j.wear.2021.203794
80. Robert F, Paulmier D, Zaïdi H, Schouller E. Combined influence of an inert gas environment and a mechanical action on a graphite surface. *Wear* **1995**, *181–183*, 687–690. DOI:10.1016/0043-1648(95)90185-X
81. Stansfield OM. Friction and Wear of Graphite in Dry Helium at 25, 400, and 800 °C. *Nucl. Appl.* **1969**, *6*, 313–320. DOI:10.13182/NT69-A28339
82. Vergari L, Quincey J, Meric de Bellefon G, Merriman T, Hackett M, Scarlat RO. Self-lubrication of nuclear graphite in argon at high temperature. *Tribol. Int.* **2023**, *177*, 107946. DOI:10.1016/j.triboint.2022.107946
83. Zaidi H, Mezin A, Nivoit M, Lepage J. The influence of the environment on the friction and wear of graphitic carbons: I. Action of atomic hydrogen. *Appl. Surf. Sci.* **1989**, *40*, 103–114. DOI:10.1016/0169-4332(89)90164-5
84. Zaidi H, Paulmier D, Lepage J. The influence of the environment on the friction and wear of graphitic carbons: II. Gas coverage of wear debris. *Appl. Surf. Sci.* **1990**, *44*, 221–233. DOI:10.1016/0169-4332(90)90053-3
85. Zaïdi H, Robert F, Paulmier D, Néry H. Correlation between the tribological behaviour of graphite and its mechanical properties versus the interplan distance. *Appl. Surf. Sci.* **1993**, *70–71*, 103–108. DOI:10.1016/0169-4332(93)90407-3
86. Zaidi H, Richard C, Bui HS, Tournis S, Aissa M, Bouguerra K. Frictional Behavior of MoS2 Coatings: AComparative Study of Dynamic and Static Friction in Vacuum and Inert Gases. *Coatings* **2025**, *15*, 500. DOI:10.3390/coatings15050500
87. Pape F. Investigation of Graphene Platelet-Based Dry Lubricating Film Formation in Tribological Contacts. *Coatings* **2024**, *14*, 360. DOI:10.3390/coatings14030360

88. Shi YQ. Benefits of nuclear power generation and status of world nuclear power development. *Energy Eng.* **2007**, 1–6. Available online: https://publish.cnki.net/journal/portal/nygc/client/paper/8b6c0a448a3f8fb871b902669475d539 (accessed on 16 August 2026).
89. Zhao CK. Development Status and Outlook for Nuclear Power in China. *Nucl. Power Eng.* **2018**, *39*, 1–3. DOI:10.13832/j.jnpe.2018.05.0001
90. Chen ZL, Gui N, Sun YF, Yang XT, Tu JY, Jiang SY. Experimental study of friction coefficient of graphite for high-temperature gas-cooled reactors. *Nucl. Eng. Des.* **2024**, *423*, 113142. DOI:10.1016/j.nucengdes.2024.113162
91. Wang SH. The Generation IV Nuclear Power and the Future of Nuclear Power in China. *Science* **2005**, *57*, 18–21. Available online: http://lib.cqvip.com/Qikan/Article/Detail?id=11698490 (accessed on 16 August 2026).
92. Yi YN. *Experimental Study on the Failure Process of Nuclear Graphite Contact Structures*; Beijing Institute of Technology: Beijing, China, 2021.
93. Liu D, Gludovatz B, Barnard HS, Kuball M, Ritchie RO. Damage tolerance of nuclear graphite at elevated temperatures. *Nat. Commun.* **2017**, *8*, 15942. DOI:10.1038/ncomms15942
94. Jiang M, Ell J, Barnard H, Wu H, Kuball M, Ritchie RO, et al. On the reduced damage tolerance of fine-grained nuclear graphite at elevated temperatures using in situ 4D tomographic imaging. *Carbon* **2024**, *222*, 118924. DOI:10.1016/j.carbon.2024.118924
95. Si MH, Gui N, Sun Y, Yang XT, Tu JY, Jiang SY. Experimental measurement of stiffness coefficient of high-temperature graphite pebble fuel elements in helium at high temperatures. *Nucl. Eng. Technol.* **2024**, *56*, 1679–1686. DOI:10.1016/j.net.2023.12.022